HELIUM EQUILIBRIUM BETWEEN PORE WATER AND QUARTZ:

APPLICATION TO DETERMINE CAPROCK PERMEABILITY

by

Stanley Devaud Smith

A thesis submitted to the faculty of
The University of Utah
in partial fulfillment of the requirements for the degree of

Master of Science

in

Geology

Department of Geology and Geophysics

The University of Utah

May 2012

The University of Utah Graduate School

STATEMENT OF THESIS APPROVAL

The thesis of **Stanley Devaud Smith**

has been approved by the following supervisory committee members:

D. Kip Solomon	, Chair	**2/15/2012** Date Approved
Brian J. McPherson	, Member	**2/15/2012** Date Approved
Thure E. Cerling	, Member	**3/1/2012** Date Approved

and by **D. Kip Solomon**, Chair of the Department of **Geology and Geophysics**

and by Charles A. Wight, Dean of The Graduate School.

ABSTRACT

The effectiveness of carbon capture and geologic storage depends on many factors, including and especially the permeability of the reservoir's caprock. While caprock integrity is generally assumed if petroleum has been preserved, it is poorly constrained in reservoirs containing only saline waters, and CO_2 leakage poses a potential risk to shallow aquifers. Naturally-occurring helium accumulates in pore waters over time with the concentration being strongly dependent on the long-term flux of fluid through the caprock. Furthermore, a small fraction of pore-water helium diffuses into quartz and this may be used as a proxy for helium concentrations in pore water, where dissolved gas samples are difficult to obtain, such as in deep sedimentary basins.

Quartz was purified from core samples from the San Juan Basin, New Mexico and the Great Artesian Basin, South Australia where pore water helium has been previously measured. Quartz separates were heated at 290°C to release helium from the quartz. The quartz from the San Juan Basin and high purity quartz from the Spruce Pine Intrusion, North Carolina was repeatedly impregnated at varying pressures using pure helium, heated and analyzed to build helium sorption isotherms. The isotherms appear linear but vary between samples, possibly due to fluid inclusions within the quartz grains as high purity quartz samples partition only 1.5% of helium that partitions into San Juan Basin samples. Concentrations of helium in the pore water were calculated using the helium-

accessible volume of the quartz and the air-water helium solubility. The mean San Juan Basin helium pore water concentration was $2x10^{-5}$ cc STP He g^{-1} water, ~400 times greater than atmospheric solubility. Great Artesian Basin samples contain a mean helium concentration of $3x10^{-6}$ cc STP He g^{-1} water or 65 times greater than atmospheric solubility. However, pore water helium concentrations in both the San Juan and Great Artesian Basins differ by up to an order of magnitude when compared to samples collected with an alternate method. The reason for the offset is attributable to either partial saturation of the pore volume or a lack of helium equilibrium between quartz and pore water. Coating of clay or other mineral phases on quartz grains, which tends to reduce the effective diffusion coefficient, may cause the latter. Modeling results suggest that helium's high mobility helps constrain formation-scale permeability including the effects of fluid flow through fractures and other seal bypass systems that may not be evident in core samples. This technique of assessing permeability is promising due to the abundance of existing core samples from numerous basins where carbon sequestration may ultimately occur.

TABLE OF CONTENTS

LIST OF FIGURES

LIST OF TABLES

Table Page

ACKNOWLEDGMENTS

This work was supported by the EPA STAR Program Award RD-83438601. High purity quartz from the Spruce Pine Pluton was provided by Unimin Inc.

I would like to thank the following people for their help in completing this work: Kip Solomon for giving me the opportunity to work on such a unique project, and for his guidance, expertise, and support throughout the process; Brian McPherson for encouragement and for thoughtful and critical editing advice; Weon Shik Han for providing a framework helium model and for helping me to get up and running with TOUGH2; Payton Gardner for providing the second set of core samples; Alan Rigby and Wil Mace for their technical help and humor in the Noble Gas Lab; Becky Hollingshaus for donuts and helping with programing and mineral separations; Scott Hynek for sharing his heavy liquid mineral separation techniques for the more difficult samples; and my wife Amanda for her love and support.

INTRODUCTION

The increase of average global temperatures over the past century has been attributed to increased concentrations of greenhouse gases in the atmosphere caused by the burning of fossil fuels. This situation has prompted the research of increased energy efficiency, using less carbon-intensive fossil fuels such as natural gas or low carbon energy sources such as renewable energy or nuclear power, and removing carbon dioxide from emission streams and preventing its release into the atmosphere (IPCC, 2005). One such developing method is to capture and compress CO_2 at the production source and transport it to long-term storage locations such as saline aquifers, depleted oil and gas reservoirs, or the ocean (IPCC, 2005). This process is generally known as Carbon Capture and Storage (CCS), and makes emission reductions feasible for fossil fuel power plants as well as energy-intensive industries, including producers of cement, ammonia, iron, and steel (IPCC, 2005).

The success of CCS in saline aquifers and depleted oil and gas reservoirs (geological storage) requires that carbon dioxide 1) is isolated from the atmosphere for thousands of years if not indefinitely, 2) is stored economically at a rate of gigatons per year to make a significant contribution to CO_2 level mitigation, as 24 $GtCO_2$ are released annually (2004 rate), and 3) does not adversely affect groundwater reservoirs used for drinking water, as dissolved CO_2 may acidify the waters and leach lead and arsenic from

the rock (Zheng et al., 2009).

Aside from a low permeability caprock acting as a seal, CCS basins require an economic reservoir volume saturated with saline water and structural simplicity (IPCC, 2005). The effectiveness of the seal or caprock is generally assumed in petroleum basins where buoyant oil and/or gas has been immobile with little to no leakage for millions or tens of millions of years. However, the use of petroleum basins for CCS offers limitations, including the storage capacity of these reservoirs is not sufficient (675-900 $GtCO_2$ including noneconomical options), and few reservoirs are currently depleted or are nearing depletion (IPCC, 2005). A larger storage capacity of at least 1000 $GtCO_2$ is found in saline aquifers, which contain water unusable for human or agricultural purposes (IPCC, 2005). However, the physical characteristics of saline aquifers and their caprocks are poorly characterized, in general, because they lack the numerous wells, geophysical surveys, and reservoir modeling that petroleum reservoirs typically possess.

One critical aspect of saline aquifer storage targets is caprock permeability. If core samples are available from the caprock, permeability and sealing capacity can be determined on individual core sample using gas permeability and mercury intrusion porosimetry, respectively. However, measurements on a single core sample may not be representative of the formation on a regional scale. The measured permeability may be a gross overestimate or underestimate of the regional permeability that may be strongly influenced by fractures and faults (otherwise known as seal bypass systems). The method presented here relies on the diffusive nature of helium, making it an effective tool for assessing permeability where extensive geologic and geophysical data are not available.

Measurement of dissolved helium and other noble gases in groundwater has been used for many studies, including $^{3}H/^{3}He$ age dating (Schlosser et al., 1988; Solomon and Cook, 2000 among others) and ^{4}He age dating (Hendry et al., 2005; Kipfer et al., 2002; Solomon, 2000; Torgersen and Clarke, 1985 among others).

Observed ^{4}He in pore waters generally originates from three sources: the atmosphere, the mantle, and radiogenic decay (Ballentine and Burnard, 2002). ^{4}He age dating relies on the subsurface production of helium by the radiogenic decay of $^{235,238}U$ and ^{232}Th producing α-particles, which gain electrons becoming ^{4}He. Atoms of U, Th, and He are generally present in minerals such as zircon, titanite, and apatite, and helium is released into the pore fluids through α-recoil, diffusion, and mineral transformations such as diagenesis and alteration (Ballentine and Burnard, 2002). Through these processes over 90% of radiogenic helium is released into pore fluids (Mamyrin and Tolstikhin, 1984). Measuring the concentration of helium in a water sample and knowing the helium production rate within a basin and the flux rate from external crustal or mantle sources, the fluid residence time may readily be determined. A calculated apparent age may not agree with helium productions rates supported by uranium and thorium concentrations due to an excess of helium from mineral alteration or residual helium concentrations (Hendry et al., 2005; Torgersen and Clarke, 1985).

Because helium is produced very slowly through radiogenic decay, the presence of high helium concentrations in pore water samples suggests that the fluid has been isolated from the atmosphere for very long periods as a result of very long flow paths in deep basins or very low fluid velocities caused by virtually impermeable sediment layers.

Measurement of pore water helium concentrations is usually accomplished using two different methods: 1) pore waters are collected while preserving the dissolved gases and 2) submerging a diffusion-type sampler and allowing the gas inside the sampler to equilibrate with the pore water dissolved gases. Both of these methods are practical and reliable for shallow groundwater studies. These methods are not practical when sampling deep low permeability formations because the low permeability layer will yield little to no water and it is typically economically prohibitive to drill a deep well and screen the well in an impermeable unit.

Osenbrück et al. (1998) developed a method to measure dissolved noble gases in pore waters coming from wells in low permeability formations that do not readily yield water. This method relies on freshly drilled cores, which are immediately subcored to remove core that is contaminated with drilling fluids and then sealed into all-metal flasks, which are then evacuated to remove atmospheric gases. Typically less than 20-30% of dissolved noble gases are lost in the process of drilling, core lifting, and container evacuation (Osenbrück et al., 1998). The dissolved gases partition into the flasks' headspace prior to analysis. The pore water volumes of the cores are determined gravimetrically.

While this method has proved to be effective and used in a few studies (Heath, 2010; Rübel et al., 2002), difficulties remain: staff must be on hand during the coring project in order to immediately preserve core samples; degassing and unsaturated pore space can cause over- or underestimations of dissolved gases.

The method tested here relies on the equilibrium partitioning of helium between

pore water and quartz within the rock matrix. Instead of relying on the collection of dissolved gases, quartz is purified from core samples and the helium contained within is released and measured. Using the helium partition ratio between quartz and water, the pore water helium concentration is determined. This pore water-quartz equilibrium was initially proposed and tested by Lehmann et al. (2003) who showed fair agreement between directly measured helium concentrations and concentrations determined using this quartz method. This study expands on Lehmann's method by applying it to shale samples whereas Lehmann used sandstone. This study also explores the variability and linearity of the helium-quartz isotherm which has received little attention aside from a few samples (Tolstikhin et al., 2005). The calculated pore water concentrations will be compared to samples collected using the canister method (Gardner et al., submitted; Heath, 2010; Osenbrück et al., 1998). If this method proves effective, it will allow the regional caprock permeability to be estimated effectively, bringing a greater degree of confidence to CCS feasibility studies.

SITE LOCATIONS

Samples were available from three sites: 1) San Juan Basin, New Mexico, 2) Great Artesian Basin, South Australia, and 3) Spruce Pine Pluton, North Carolina.

San Juan Basin

Core samples from the San Juan Basin were taken from the Pump Canyon Site in the north central portion of the basin, coinciding with the northeast trending Fruitland Fairway. This site was studied because pore water helium was measured by Heath (2010) using the canister method (Osenbrück et al., 1998). In the spring of 2008 ten samples were subcored from two core sections of the CO_2 injection well EPNG Com A Inj. #1 (Heath, 2010). The well targets the Fruitland Formation and cores were taken from the upper and lower members of the overlying Kirtland Formation.

The San Juan Basin is located in northern New Mexico and southern Colorado and covers approximately 19,000 km^2. This structural basin contains sedimentary rocks from the Cambrian to Quaternary with thicknesses up to 4,500 m with up to 1,800 m being from the Late Cretaceous when the San Juan Basin sat on the margin of the Western Interior Seaway and underwent multiple transgression-regression cycles (Fassett and Hinds, 1971). Samples were available from the Upper Cretaceous (73-74.4 Ma) Kirtland Formation. The Kirtland Formation is composed of sandstone, siltstone, shale,

and claystone deposited in alluvial and fluvial environments (Fassett and Hinds, 1971). The Kirtland Formation can be divided into a lower shale member (0-140 m) overlain by an upper shale member (0-450 m) that locally contains the Farmington Sandstone member at the base. The Kirtland Formation overlies the Fruitland Formation conformably through most of the basin. The Fruitland Formation is coal-rich and is a major source of coalbed methane. The Tertiary Ojo Alamo Sandstone overlies the Kirtland Formation throughout most of the basin with the exception of younger Tertiary rocks in the northern part (Fassett and Hinds, 1971).

The hydrogeology of the San Juan Basin surrounding the Pump Canyon Site have been described by 2-D and 3-D modeling, primarily to understand the Fruitland Formation (Kaiser et al., 1994; Kernodle, 1996). In the area of the Pump Canyon drill site, the Fruitland Formation has artesian overpressure caused by topographic forcing. Water is recharged to the north in Fruitland Formation outcrops. Direct measurement of permeability in the Farmington Sandstone range from $6x10^{-16}$ to $9x10^{-15}$ m^2. Two-dimensional modeling best-fit permeability of the Kirtland Formation members is 10^{-17} m^2 for the upper and lower shale members and 10^{-16} m^2 for the Farmington Sandstone. The hydraulic head gradient is vertical at ~1.8 m m^{-1} near the Pump Canyon Site, exceeding hydrostatic gradient and indicating upward flow.

Great Artesian Basin

A second set of core samples was available from the Great Artesian Basin (GAB), Australia. This site was chosen because pore water helium was measured in two wells

(described below) by Gardner et al. (submitted) using the canister method (Osenbrück et al., 1998). The Great Artesian Basin is a substantial Mesozoic sedimentary basin that underlies 22% of the continent and contains important water resources (Shepard, 1978). The basin sits in the eastern portion of the continent and is bound by the Great Dividing Range to the east and the Australian deserts to the west (Bethke et al., 1999). As an important water resource of the continent the GAB has been studied extensively including the measurement of dissolved noble gases (Bethke et al., 1999; Mazor, 1995; Mazor and Nativ, 1994; Torgersen and Clarke, 1985). Two primary confined aquifers of Jurassic (J aquifer) and Cretaceous (K aquifer) are overlain by a thick Cretaceous aquitard. Recharge to the aquifer occurs primarily in the Great Dividing Range and generally flows southwest with deep, long flow paths.

Samples were taken from the Nancy's Bore and Birthday Bore wells in northern South Australia. The wells penetrate the Cretaceous aquitard sequence overlying the primary aquifers. The aquitards are marine-deposited and primarily composed of shale (Shepard, 1978). The Birthday bore contains the Early Cretaceous Bulldog Shale while Nancy's bore contains approximately 160 m of Bulldog Shale overlain by 8 m of Coorikiana Sandstone followed by 125 m of Early Cretaceous Oodnadatta Shale. The hydraulic gradient is approximately 1.0 (m m^{-1}) and oriented vertical in this discharge zone. Permeability of the aquitard has been determined at 10^{-21} m^2 (hydraulic conductivity = 10^{-14} m s^{-1}). Isotopic data suggest that the flow system has been in place for at least 400,000 years (Gardner et al., submitted).

Spruce Pine Pluton

Ultra high purity quartz was available for this study as a comparison to "natural" quartz removed from shale cores. The purity of this quartz makes it suitable for electronic manufacturing and is mined from pegmatite granitoids in the Spruce Pine Plutonic Suite, North Carolina by the Unimin Corporation (Swanson and Veal, 2010). The pluton was emplaced approximately 400 Ma based on whole rock Rb-Sr ages.

MATERIALS AND METHODS

Sample Descriptions

Ten samples came from the Kirtland Formation of the San Juan Basin, New Mexico. Five samples were retrieved from the upper Kirtland formation at depths between 625 and 629 m and an additional five samples retrieved from the lower Kirtland formation at depths between 820 and 822 m. The coring program intended to take 18.29 m of core in these two formations but difficulties in coring resulted in much less recovery (Heath, 2010). The cores were subsampled parallel to the core axis at 0.5-1.5 m intervals and sealed in a stainless steel vacuum canister for dissolved noble gas analysis (Heath, 2010). Each sample was 2.5 cm wide and approximately 8.0 cm long with a weight of approximately 150 g.

Fifteen samples were available from the Great Artesian Basin and come from two wells: three samples from the Birthday borehole at 30, 60, and 90 m depth, 12 samples from Nancy's borehole spaced roughly evenly from 35 m to 290 m depth. All samples are grey shale or sandy shale. Each ~60 g sample was a subcore, taken perpendicular to the original core axis. This original subcoring was done to measure dissolved noble gases similar to the method of Osenbrück (1998).

High purity quartz samples from the Spruce Pine intrusion were heavily processed through acid leaching and other processes to remove impurities. Visual inspection by

optical microscope showed no signs of other mineral phases and very few fluid inclusions.

Experiment Design

Analysis of helium released from quartz required that the sample size was large enough to obtain a measureable amount of helium using existing instrumentation and that helium could be released from the quartz within a practical time period. The diffusivity of helium in natural quartz samples was measured by Trull et al. (1991) who found stepwise heating of the quartz yielded a smooth release of helium indicating volume diffusion from the quartz as opposed to surface site release. The resulting diffusivity of helium is given by the temperature dependent Arrhenius equation:

$$D = D_0 e^{-E_A/RT}, \quad (1)$$

where D is the diffusivity ($m^2\ s^{-1}$), D_0 is the maximum diffusivity ($1.58 \times 10^{-4}\ m^2\ s^{-1}$), E_A is the activation energy (105 kJ mol^{-1}), R is the gas constant (J $mol^{-1}\ K^{-1}$), and T is temperature (K). Assuming spherical quartz grains of radius r, the characteristic time t for equilibrium release or impregnation can be calculated using:

$$t = \frac{r^2}{D}. \quad (2)$$

Figure 1 shows that the characteristic time varies over several orders of magnitude as

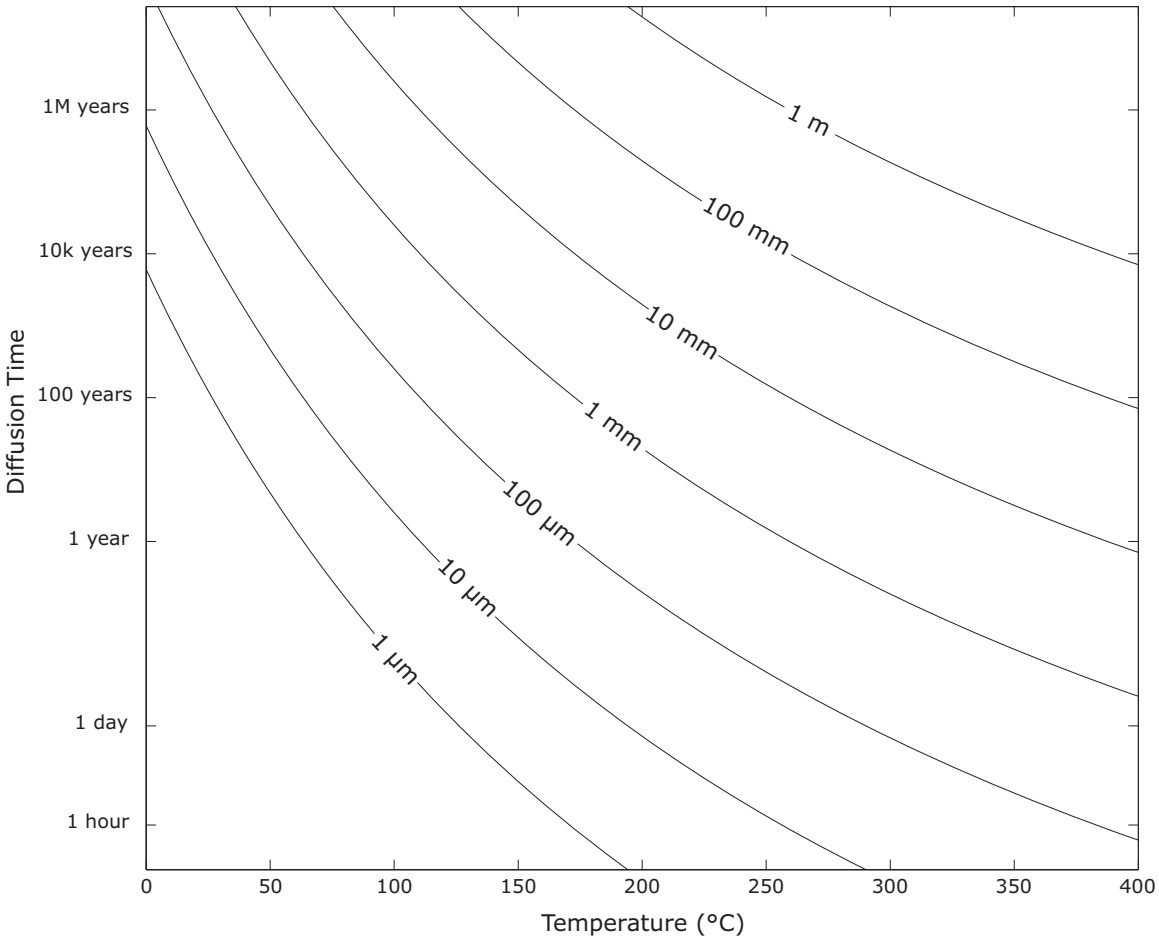

Figure 1: Equilibrium diffusion time for spherical quartz grains with diameters ranging from 1 micron to 1 m.

temperature changes from 0-400°C. For example a 1.0 mm diameter sphere would reach equilibrium with helium in several days at 400°C or millions of years at 50°C. These equilibrium calculations were verified by a analytical spherical diffusion model (Crank, 1975) that assumes a homogenous distribution of helium as an initial condition and a constant boundary concentration.

A consideration of grain size was necessary in the aspects of *in situ* and laboratory equilibrium time as well as the number of grains recoverable from a shale core sample weighing 50-200 g. A grain size range of 44-150 μm (coarse silt – fine sand; 325 and 100 U.S. standard sieves) can be separated from 90% of San Juan Basin samples (9/10) and 80% of GAB samples (12/15). The remaining samples were finer grained. At this size fraction and at laboratory temperature of 290°C, the characteristic time ranges from 5.0 to 55 hours. At an environmental temperature of 25°C the characteristic time ranges from 0.1 to 2.9 million years. Modeling of diffusion in a spherical quartz grain with a radius of 75 μm and an initially homogenous distribution of helium using the analytical solutions of Crank (1975) suggests that in the characteristic time 99.997% of helium has been lost from the grain. Erring on the side of caution to avoid multiple analyses, a time of 10 days (4.4 characteristic time lengths) was used for every sample to ensure all helium was released into the headspace. Furthermore, 12 samples were placed in the oven for an additional 10 days after analysis and then analyzed a second time and this verified that the helium was completely released.

The laboratory temperature of 290°C was chosen for the short times required to release and impregnate quartz but also to preserve quartz defects such as inclusions that

could hold significant amounts of helium. Lehmann et al. (2003) performed step-wise heating experiments from 200°C to over 1700°C to observe the release of helium from quartz and found that below 350°C, a negligible amount of helium was released during 45 minute time steps suggesting that this temperature is an upper limit for releasing helium without irreversibly affecting the grains. Lehmann's impregnation and release experiments were ultimately carried out at 290°C and for comparison, this study will use the same temperature.

The *in situ* equilibration time needs to be considered, as the pore water helium concentrations are not expected to be constant for millions of years. An environmental temperature of 25°C is an appropriate minimum temperature when considering the requirements of CCS projects. To efficiently store CO_2 in reservoirs of limited volume, the temperature and pressure must be great enough that CO_2 remains as a dense supercritical phase (Figure 2). Assuming a geothermal gradient of 25°C km^{-1} this depth is approximately 800 meters and with a mean annual temperature of 5°C at the surface, 25°C is present at 800 m (IPCC, 2005).

The *in situ* equilibration time of 2.9 million years presented above needs to be addressed as hydraulic systems may not be that long-lived when considering variability of climate, recharge to the system, and the evolution of permeability. Consider that helium is released into the pore water at an initial rate supported by typical uranium and thorium concentrations ($2.4x10^{-12}$ cc STP He g^{-1} yr^{-1}). Over time pore water helium will reach equilibrium, as the helium lost through diffusion is equal to helium added through radiogenic decay. If the pore water equilibrium concentration is 10^4 greater than the

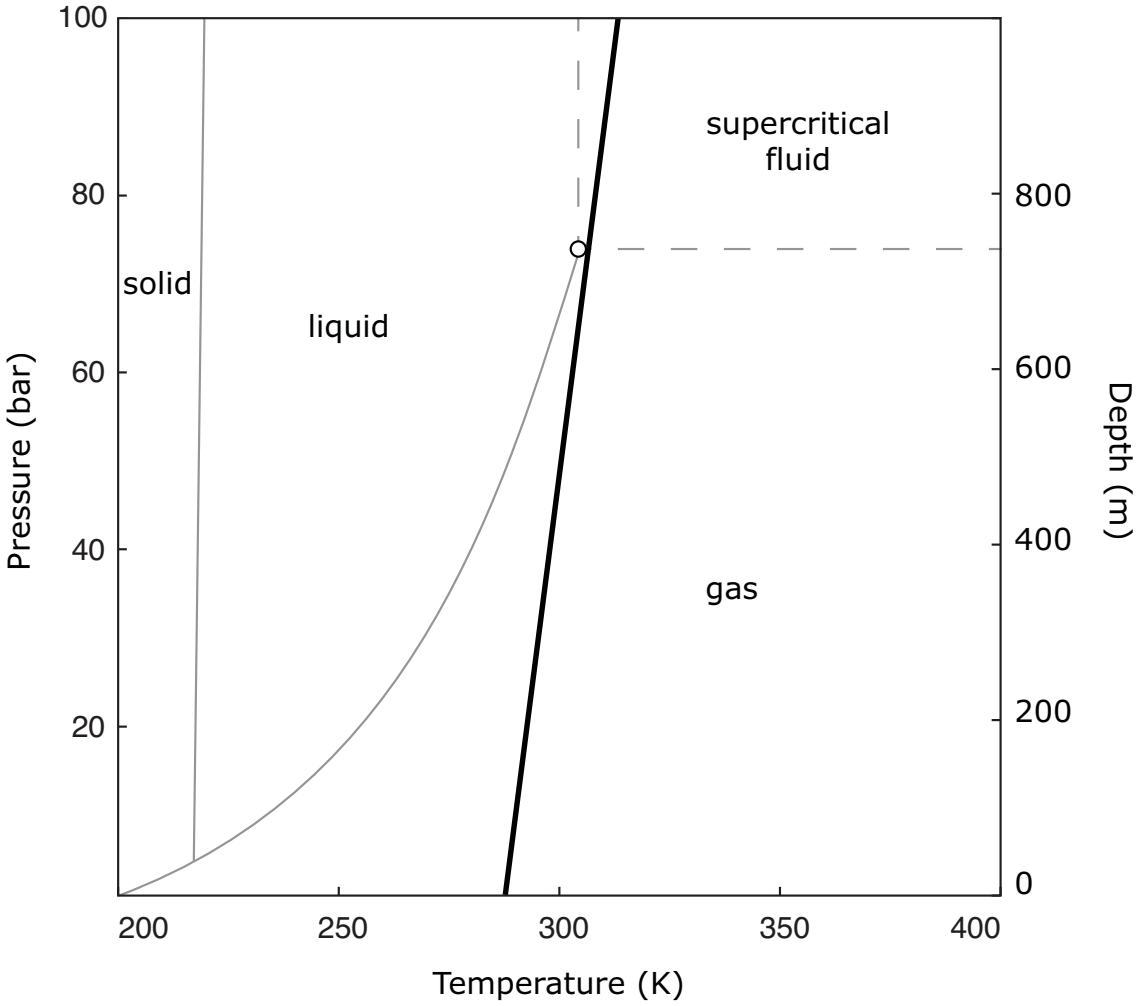

Figure 2: Phase diagram for carbon dioxide. Shown in bold is a 25 K km^{-1} geothermal gradient, assuming hydrostatic pressure and a surface temperature of 288 K.

initial concentration, the quartz helium concentration lags behind the pore water helium concentration and after approximately 1.9 million years the 150 μm quartz grains will have a helium concentration that is 90% equilibrated with the pore water (Figure 3). Because it is unlikely that helium concentrations will change rapidly, quartz-water helium equilibrium will be near complete provided that sediments are significantly old. With this information, an equilibration time of 2.9 million years is negligible when analyzing Cretaceous-aged sediments of the San Juan and Great Artesian Basins.

Sample size needs to be large enough that accurate measurements can be made but small enough that sensors do not become saturated during measurement, leading to nonlinear measurements. A reference gas of atmospheric composition was used for calibration and produces a measurement of approximately 1 volt of helium-4. Using the sample pressure, volume, and molar fraction, 4.9×10^{-11} moles He are in the standard aliquot. Average blank measurements are on the order of 10^{-4} volts. To make a measurement 10% of the standard, 1 g of quartz needs to contain 4.9×10^{-12} moles He or 1×10^{-7} cc STP He. This amount seems reasonable when the samples we intend to analyze contain pore water concentrations of $\sim 5 \times 10^{-5}$ cc STP He g^{-1} (Heath, 2010) and estimates of noble gas (Ar and He) partitioning between pore water and minerals would suggest quartz helium concentrations of 5×10^{-8} cc STP He g^{-1} (Brooker et al., 1998).

The diffusivity of other common minerals that may contain helium was considered to assess the degree of mineral purity necessary. Minerals that produce and retain helium from internal U and Th decay include apatite, zircon, monazite, and titanite (Baxter, 2010). At 290°C the diffusivity of helium in zircon, monazite, and titanite are six to eight

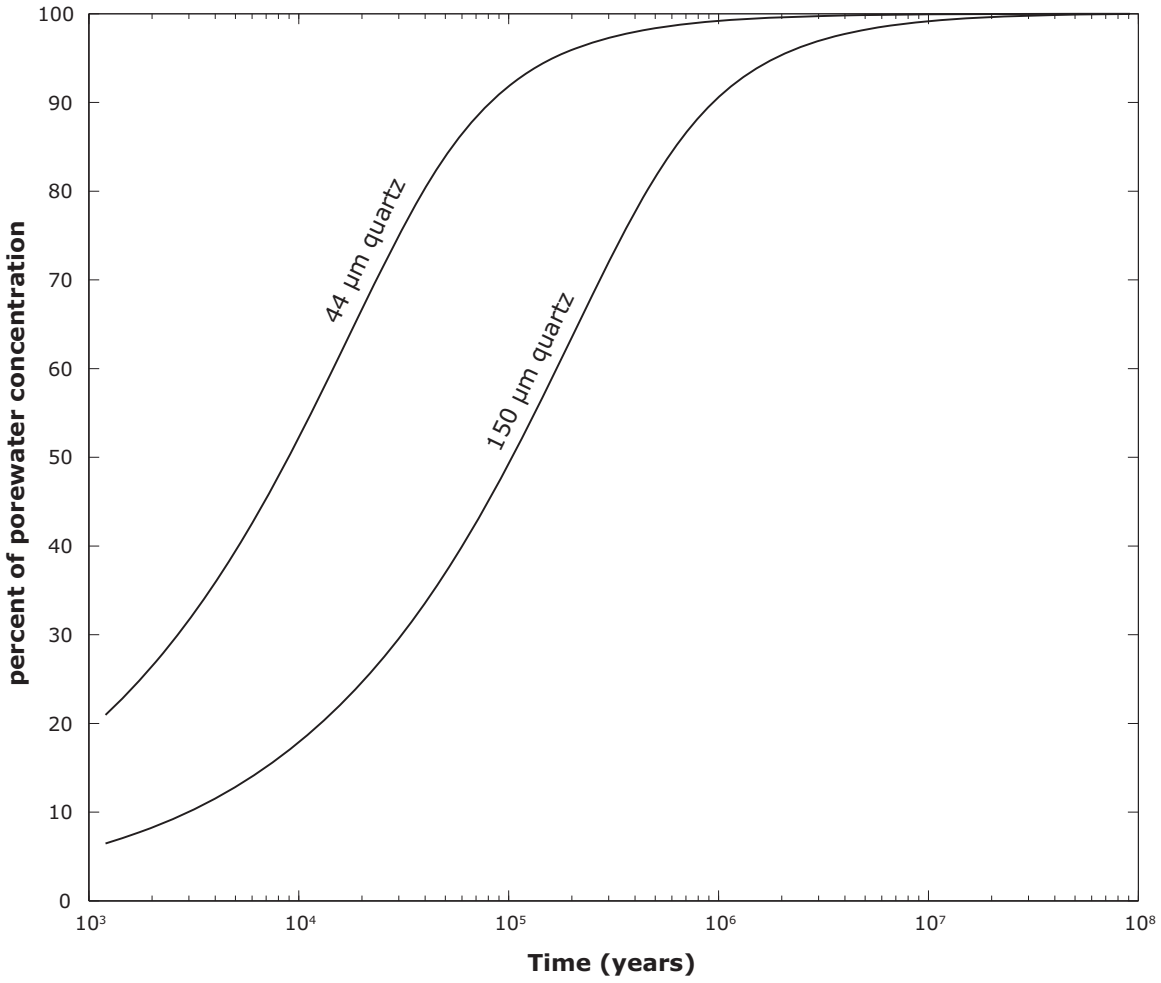

Figure 3: Spherical quartz grain helium concentration relative to pore water concentration. This assumes no partition ratio between the quartz and pore water.

orders of magnitude smaller than quartz suggesting that these minerals would contribute very little helium during laboratory heating (Baxter, 2010). Apatite, however, has a diffusivity approximately two orders of magnitude larger than quartz at 290°C (Baxter, 2010; Farley, 2000). This difference in diffusivity proves important when considering that apatite is generally nonreactive and has a low magnetic susceptibility similar to quartz (Rosenblum, 1958). When heated over the 10 day period a 150 μm spherical grain of apatite with a homogenous helium distribution could lose 71% of internal helium, while virtually all helium would be lost from a 44 μm apatite grain. Furthermore the diffusivity of helium in apatite at 25°C is four orders of magnitude greater than that of quartz suggesting that helium equilibrium between apatite and pore water will not occur.

Mineral Separation

The goal of mineral separation was to isolate quartz from the other mineral phases that may: 1) contain abundant amounts of U and Th and thus He, including titanite, apatite, and zircon as mentioned above, or 2) may partition helium differently than quartz. During this extraction, mechanical processing was to reduce fracturing of quartz grains which could release helium adjacent to the fracture (Ballentine and Burnard, 2002).

Approximately 50 g from each San Juan Basin sample was roughly disaggregated into approximately 1 cm^3 pieces using a porcelain mortar and pestle in order to fit into a Shatterbox, a shaker containing concentric tungsten carbide rings, to pulverize the samples. Shaking for 15-20 seconds in the Shatterbox proved effective for reducing the

sample to a powder. The samples were then dry-sieved at 850, 150, and 43 μm using standard sieves. The fraction smaller than 43 μm was discarded while the larger-than-850 μm fraction was further disaggregated using a mortar and pestle before resieving. A typical 50 g sample yielded 15-20 g at the 44-150 μm size-fraction without relying on excessive reworking with the mortar and pestle.

The sought-after size fraction was then rinsed in deionized water to remove any residual clay particles before carbonates were removed using 10% nitric acid and agitating for 5 minutes in an ultrasonic bath. Clay and feldspar minerals were removed using 5% hydrofluoric acid. Because hydrofluoric acid will dissolve quartz, samples were rinsed in deionized water, dried in a 70°C oven, and examined under a microscope to determine how much clay remained on the quartz before more hydrofluoric acid was added.

Quartz was further isolated magnetically. A Frantz isodynamic magnetic separator was used to remove all minerals that have any slight magnetism. Using a high magnet amperage (1.7) and 5-12° side tilt, most minerals are separated from quartz. Rosenblum (1958) found that with 100-150 μm particles, 25° forward tilt, 15° side tilt, and 1.7 amps several minerals remain unaffected by the magnetic field. These include all quartz, and some feldspar, zircon and apatite. After magnetic separation, quartz purity was generally satisfactory with <5% feldspar excluding a few samples that contained higher levels of feldspar or a lower density black substance. This black substance was partially removed using heavy liquids due to the difference in density. These poor separations were ultimately not analyzed for helium.

Samples from the Great Artesian Basin were processed in a similar manner as

described above. GAB samples were less lithified and were processed in the Shatterbox for less time (~8 seconds), which was followed by wet sieving at the 43 and 150 μm sieve sizes. Acid and magnetic treatments were the same as described above for San Juan Basin samples.

Ultra high purity quartz samples from the Spruce Pine Pluton required no processing aside from sieving to the 44-150 μm size fraction. Four g of quartz were split into four equal fractions and analyzed separately.

Sampler Design

The quantitative analysis of helium released from the quartz required that the internal volume of the sampler could 1) be held at high vacuum and specific pressures, 2) be able to withstand temperatures of 290°C for multiple days, and 3) be easily compatible with existing setup in the Dissolved and Noble Gas Laboratory at the University of Utah.

The samplers are made of 16 cm sections of 0.25" (6.35 mm) refrigeration grade copper tubing; each was crimped and silver soldered shut on one end, and flared and fitted with an AN fitting on the other (Figure 4). Samplers were cleaned by boiling in deionized water, rinsing with ethyl alcohol, and the inner surface wiped with a lint-free tissue before drying. The samplers were then weighed on an analytical balance before the quartz was added. Approximately 1 g of purified quartz was added to the sampler before a 10 micron grade 316 stainless steel frit was inserted and crimped in place. The frit serves two purposes: 1) prevents quartz from being lost during high vacuum pump-down and 2) prevents quartz grains from enter the clamping area, which could prevent a

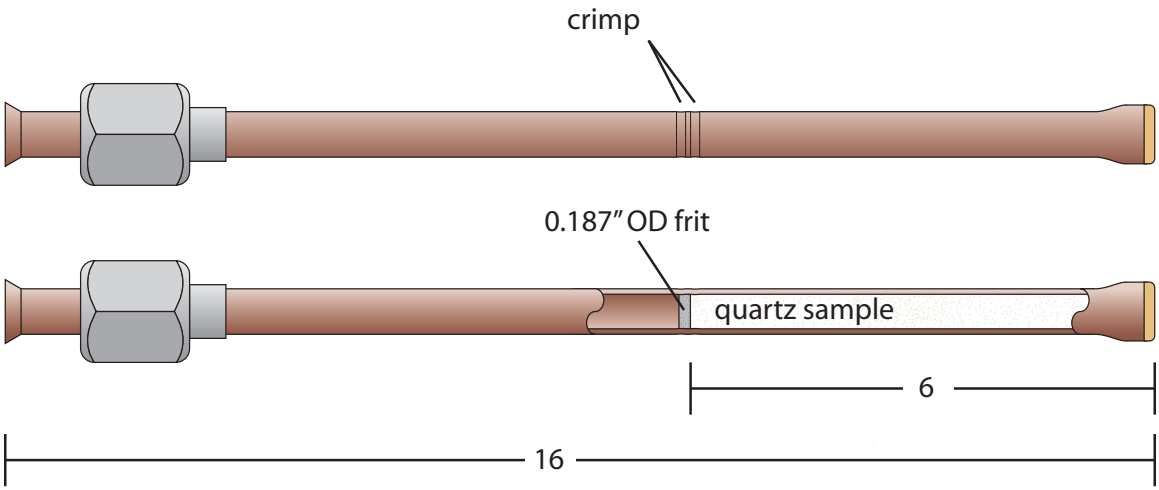

Figure 4: Sampler design. Units in cm unless otherwise noted.

vacuum tight seal.

Samplers were evacuated of all atmospheric gas for 24 hours using an all-metal extraction line attached to a turbo vacuum pump backed by a roughing pump. Samplers were then sealed on-line using stainless steel pinch-off clamps custom designed for sealing refrigeration grade tubing. Sealed samplers were then placed in a 290°C oven for 10 days causing an equilibrium partitioning of helium between the quartz and the headspace. This was followed by analysis of the noble gases released into the headspace as described below.

After helium release and analysis, effectively all helium was removed from the quartz and headspace even though a very small amount of helium remained partitioned to the quartz. This amount attributed to less than 1% of the helium initially released as determined by analyzing samples after an additional 10 days at 290°C. In order to assess how much helium the quartz can contain versus how much was measured, all samples were impregnated with helium. The sampler headspace was purged and filled with ultra high purity (99.999%) helium at pressures between approximately 0.5 and 100 Torr at room temperature (22°C). Using the ideal gas law, these pressures rise by a factor of 1.9 when heated from 22°C to 290°C resulting in impregnation pressures between 0.95 and 190 Torr. The accuracy of pressure measurements was 0.001 Torr and 1 Torr for pressures below and above 10 Torr, respectively. The samplers were then resealed and heated at 290°C for an additional 10 days causing helium to partition between the quartz and the headspace. Calculations indicate that the total mass of helium partitioned to the quartz was not great enough to change the headspace helium pressure (calculations not presented). After impregnation, the quartz was transferred to a new sampler in the case

that helium had partitioned to the copper walls or the stainless steel frit. A single empty sample was prepared to test this hypothesis and showed that at 42 Torr impregnation pressure yielded 0.39 volts ^{4}He, which is approximately 20% of what a quartz sample at this pressure ultimately yielded. At this point the samplers were evacuated of atmosphere for 24 hours as described above, and heated for 10 days at 290°C to release the helium added through impregnation. This impregnate-and-release process was repeated three-five times for each sample at varying helium pressures in order to determine the linearity of the isotherms. Previous impregnation experiments (Lehmann et al., 2003) were completed at a single pressure of 32 atmospheres (24,320 Torr) which is much greater than pressures seen in nature and does not assess the linearity of helium partitioning to helium. If the helium-quartz system is similar to solutes-solid systems, higher concentrations show saturation, at which point the media can no longer sorb additional molecules (i.e., Langmuir isotherms).

Noble Gas Analyses

Gases released from the quartz grains were analyzed at the Dissolved and Noble Gas Laboratory at the University of Utah, Salt Lake City, Utah. Each sample was inlet into a clean up line before all noble gases and their isotopes, excluding helium, are analyzed on quadrupole mass spectrometer. Due to a line volume difference between standard and sample analysis runs, only neon can be compared to standard concentrations. Helium (^{3}He and ^{4}He) was analyzed on a MAPL 215-50 magnetic sector field linear mass spectrometer. Gas volumes from seven samples impregnated at high helium pressures were split into 10% or 50% aliquots before being inlet due to high

helium concentrations. The precision of analysis was approximately 1% for He and 2% for neon. While neon was not expected to be released from the quartz, it served as an indicator of atmosphere leaking into the sampler as discussed below.

RESULTS AND DISCUSSION

Leak corrections

The helium measurements were leak-corrected using several methods before ultimately understanding the nature of the leakage. Samples were considered contaminated with atmosphere if the R/R_a (the ratio between the measured $^3He/^4He$ ratio and the atmospheric $^3He/^4He$ ratio) was higher than expected and/or the $^{20}Ne/^{22}Ne$ ratio was near atmospheric. Gas leaked into sample containers was initially considered of atmospheric composition; the result being a binary mixture of atmosphere and helium released from the quartz. The atmospheric composition end-member contains a known ratio between helium-3 and helium-4 as well as helium-4 and neon-20. As stated above, it was assumed that neon is not released from the quartz. If the measured ratio between ^{20}Ne and ^{22}Ne was near atmospheric ($^{20}Ne/^{22}Ne = 9.80$), atmospheric helium can be corrected using a method similar to Schlosser (1992):

$$^4He_r = {}^4He_{meas} - Ne\left(^4He/Ne\right)_{atm}, \quad (3)$$

where ^4He_r is the radiogenic helium, $^4He_{meas}$ is the amount of helium measured, Ne is the total neon measured, and $\left(^4He/Ne\right)_{atm}$ is the helium-neon atmospheric ratio (0.288). Similarly this approach can be used calculate the $^3He/^4He$ ratio attributed to the

quartz only, or

$$\left({}^{3}\mathrm{He}/\,{}^{4}\mathrm{He}\right)_{r} = \frac{{}^{3}\mathrm{He}_{meas} - \mathrm{Ne}\left({}^{3}\mathrm{He}/\mathrm{Ne}\right)_{atm}}{{}^{4}\mathrm{He}_{r}}, \quad (4)$$

where $\left({}^{3}\mathrm{He}/\mathrm{Ne}\right)_{atm}$ is the atmospheric ^{3}He/Ne ratio (3.98×10^{-7}). However, when the results of Eqn. 4 were compared to impregnation experiments, where the correct ^{3}He/^{4}He ratio was known, Eqn. 4 gave ratios that were up to a factor of 2.5 greater than expected (Figure 5). This suggests that the ^{4}He/Ne ratio of leakage was not atmospheric and that a deficit of neon is implied.

An alternative approach to leak-correction was to ignore the neon concentrations and instead only use the ^{3}He/^{4}He ratio. When the helium ratio was nonatmospheric and known *a priori*, such as when impregnating quartz with a helium source with a characterized helium isotope ratio, the measured concentration was treated as a binary mixture of helium from impregnation and from the atmosphere:

$$R_{meas} = R_{sample}X_{sample} + R_{a}X_{leak}, \quad (5)$$

$$X_{sample} + X_{leak} = 1, \quad (6)$$

where R_{meas} is the measured ^{3}He/^{4}He ratio, R_{sample} is the ^{3}He/^{4}He ratio of the impregnation source (2.1E-7 to 2.8E-7 in these experiments), R_a is the atmospheric ^{3}He/^{4}He ratio (1.38E-6), and X_{sample} and X_{leak} are the mass fractions helium from the released from the sample and from the atmosphere, respectively. Eqn. 5 and 6 are rearranged and ultimately

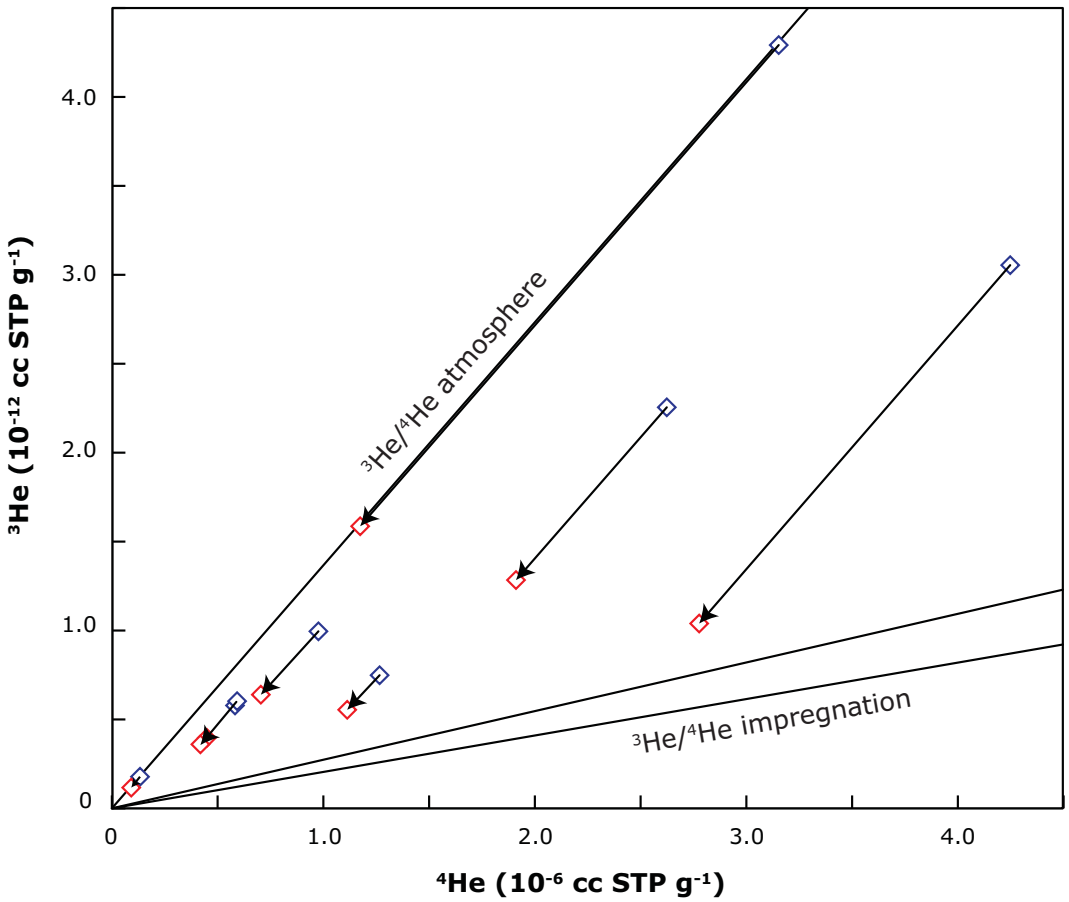

Figure 5: Atmospheric He/Ne ratio correction applied to leaky samples. Note that the corrected concentration should plot on one of the lower lines. Because this was not observed, this model is incorrect.

give:

$$^4He_{sample} = {}^4He_{meas}\frac{R_a - R_{meas}}{R_a - R_{sample}}. \quad (7)$$

This correction method gives a better result but the question remains as to why the neon correction does not give the same result. A neon deficit was calculated for each leak using the R/R_a correction results. It was found that the measured neon-20 was 37-76% of what was expected when compared to helium-4 (Figure 6).

To determine if this apparent neon deficit was caused by a measurement error such as a nonlinearity of quadrupole mass spectrometer neon measurements, samples of atmospheric composition were split to fractions of 100, 16, and 2%. Comparing the 100% and 2% splits, there is a slight nonlinearity between helium-4 and neon-20, with the $^4He/^{20}Ne$ ratio increasing 9%. This degree of error is not large enough to explain the observed helium-neon relationship.

A possible reason for this discrepancy appears to be a difference in effusion rates between helium and neon. With a factor of five mass difference, Graham's Law (Graham, 1864) says that the helium-4 effusion rate is a factor of 2.24 greater than neon-20. It has been observed in leaking samples that small leaks have the largest $^4He/^{20}Ne$ ratios and large leaks have $^4He/^{20}Ne$ ratios approaching the atmospheric ratio. This information suggests that using neon to correct for leaks is not appropriate. In addition it should be noted that in the event of a leak, ^3He effuses faster than ^4He by a factor of 1.15, thus causing an appreciable enrichment of ^3He. Therefore, the leak correction cannot be made assuming the gas leaking in has an atmospheric ratio.

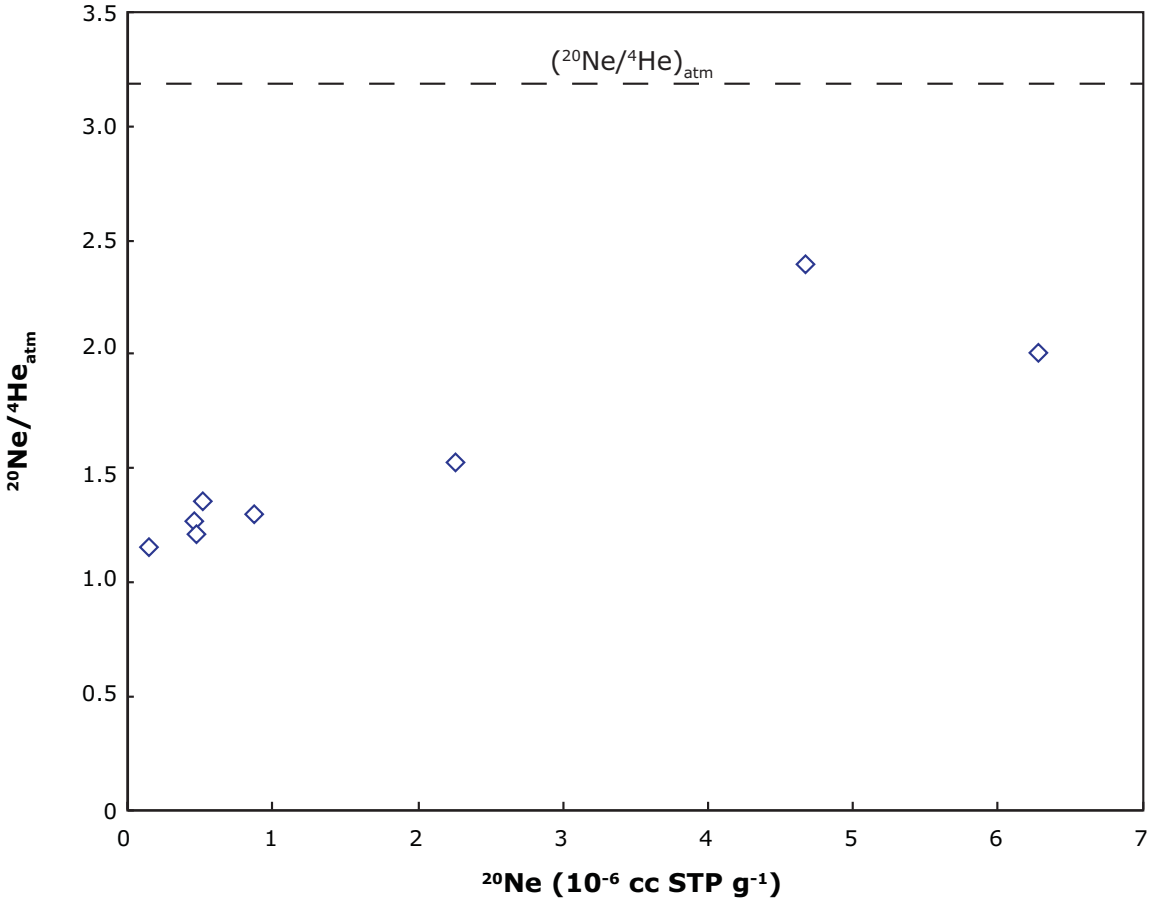

Figure 6: Atmospheric $^{20}Ne/^{4}He$ ratio compared to measured neon-20 concentration. The smallest leaks show the largest deficit of neon while larger leaks appear to approach the atmospheric $^{20}Ne/^{4}He$ ratio.

To address this problem, a different model was considered in which the input rate of individual gases from the atmosphere was a function of their relative masses. Furthermore, the gases follow an ingrowth-type curve suggesting that larger leaks show less fractionation (Figure 7). The correction was applied by first calculating the atmospheric leak of helium using Eqn. 7 and assuming R_a=1.38x10^{-6}; the neon deficit was calculated assuming an atmospheric He/Ne ratio, and this amount of neon deficit was used to determine a helium-3 excess and thus a value to replace the R_a value used in Eqn. 7. The calculations were iterated until the helium-3 excess and neon-20 deficit matched for a given relative leak size. The result shows that leaky samples had atmospheric helium R/R_a values between 1.02 and 1.15 with neon deficits between 0.45 and 0.77 (Figure 8).

An analysis of ^{3}He/^{4}He ratios as they relate to impregnation pressure shows that samples with the lowest impregnation pressures had the highest ^{3}He/^{4}He ratios and thus the largest fraction of atmosphere (Figure 9). It is suggested that impregnation experiments be performed at pressures above approximately 10 Torr to minimize the effects of atmospheric leakage. Above 10 Torr, leak corrections were generally unnecessary or removed less than 1% of the total helium. In contrast, below 10 Torr, leak corrections generally accounted for a few percent of the measured helium, while a few samples with very low impregnation pressures contained up to 95% leaked helium.

Initial helium release

San Juan Basin samples yielded between 9.9x10^{-8} and 2.9x10^{-6} cc STP He g^{-1} with a median value of 4.6x10^{-7} cc STP He g^{-1} (Table 1). Samples from the Upper Kirtland

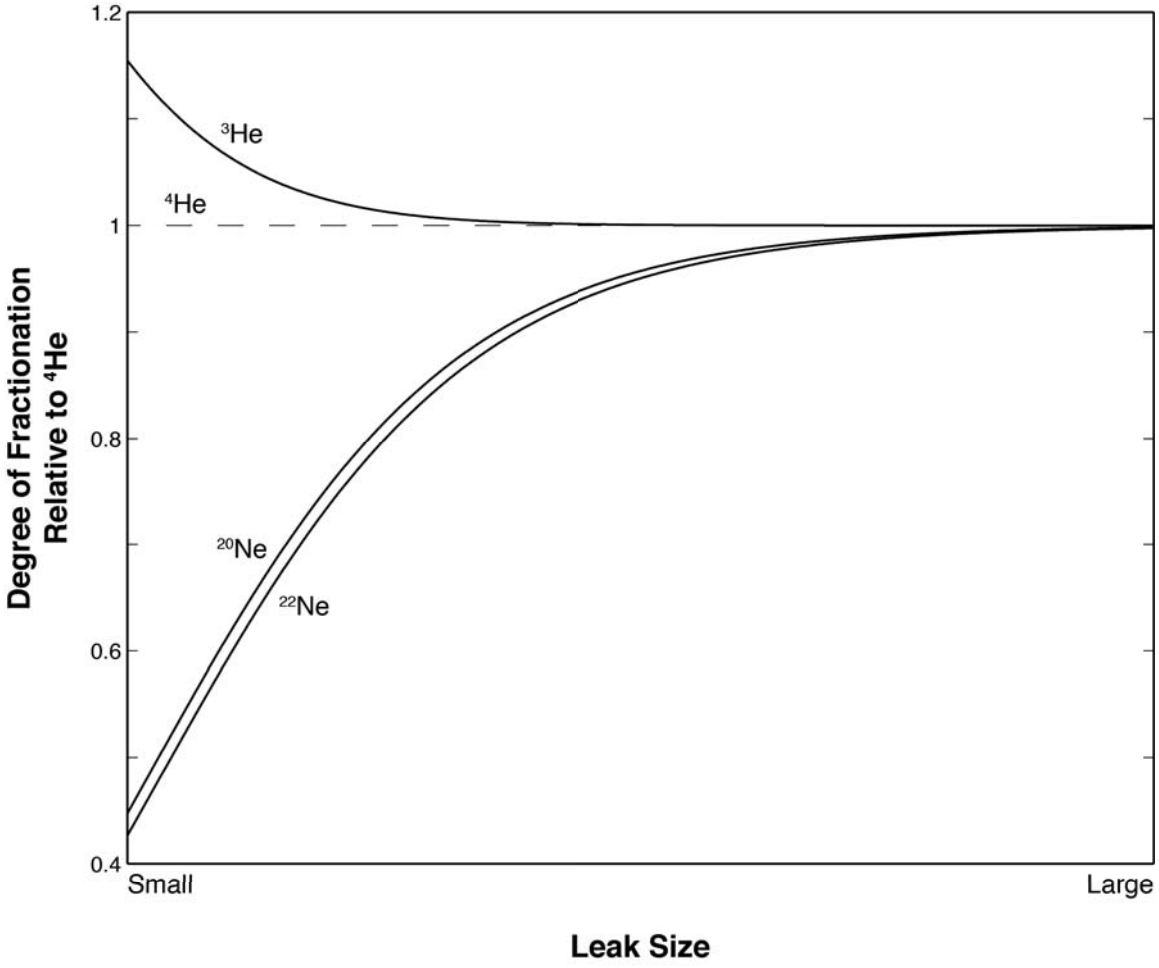

Figure 7: Helium-3 excess and neon deficiency relative to helium-4 due to mass dependent effusion rates.

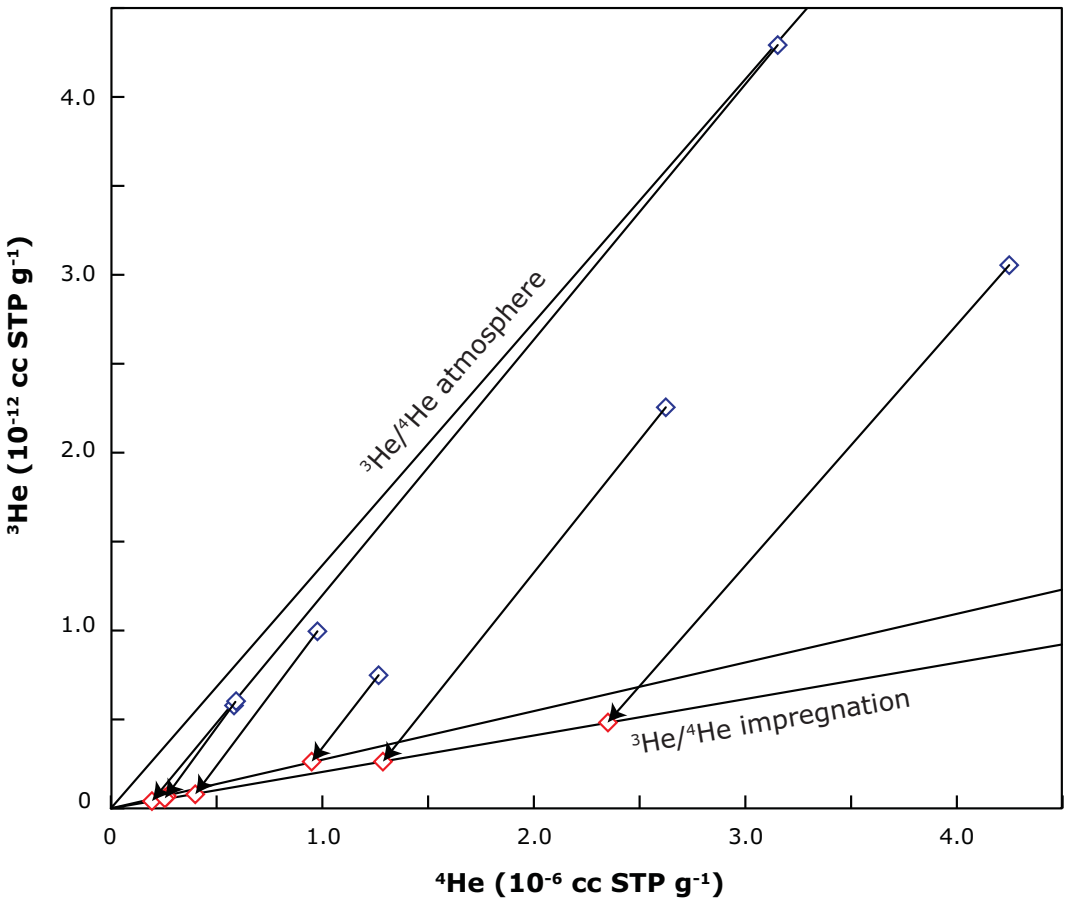

Figure 8: Leakage corrections considering different effusion rates between neon and helium. This accounts for the apparent neon deficit.

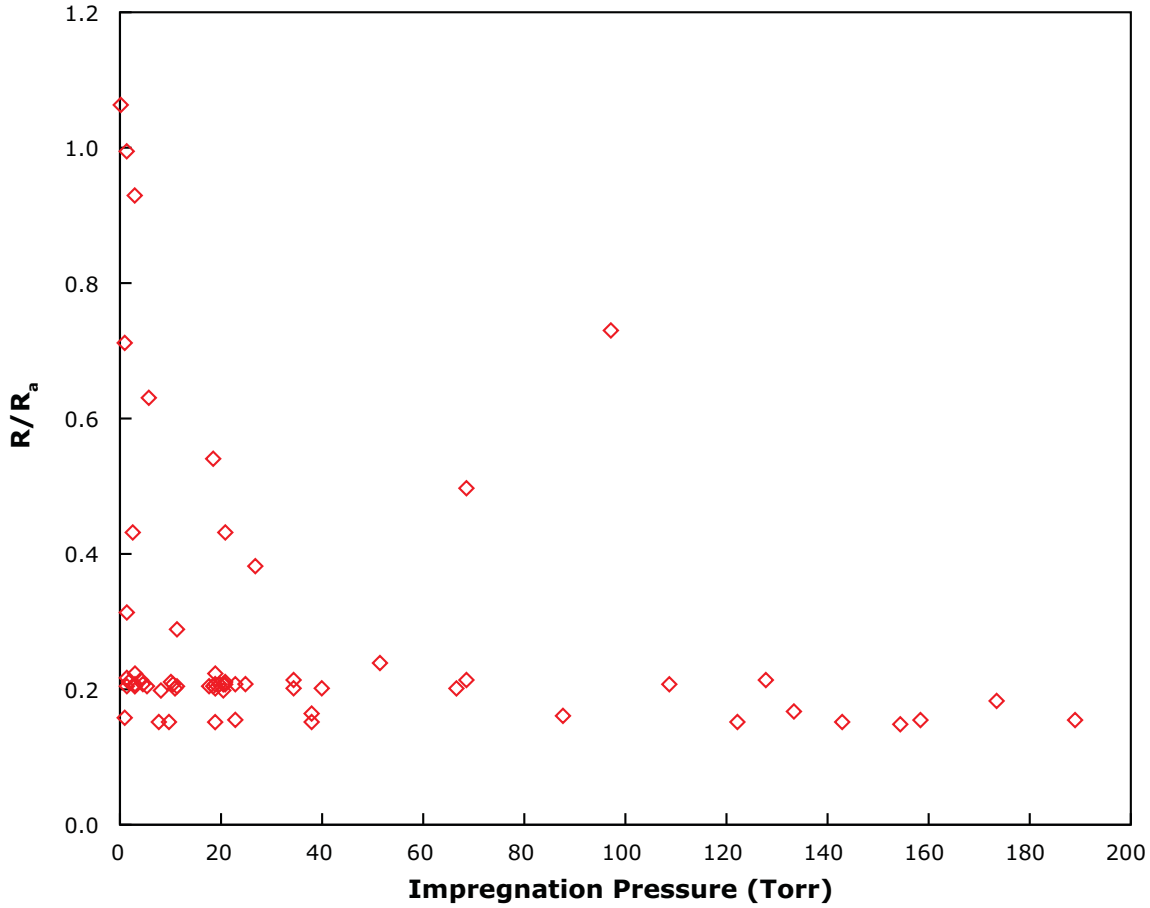

Figure 9: Helium ratio related to impregnation pressure. Samples impregnated at 20 Torr and higher have little chance of being dramatically effected by atmospheric leakage. The outliers in the middle of the graph represent Spruce Pine Intrusion samples, which uptake ~1.5% helium compared to San Juan Basin samples. The grouping of data at R/R_a values of 0.15 and 0.20 are due to the use of different helium tanks with different R/R_a ratios.

Table 1: Initial helium release data

	Sample	^{4}He cc STP cm^{-3} (x10^{-7})	^{3}He/^{4}He ratio (R/R$_a$)	^{20}Ne cc STP cm^{-3} (x10^{-8})	^{22}Ne cc STP cm^{-3} (x10^{-8})
San Juan Basin	626.70 m	76.2	0.151	4.70	2.05
	626.70 m Dup	74.2	0.150	0.09	1.29
	628.22 m*	23.2	0.175	33.6	5.29
	629.14 m*	19.7	0.173	40.1	4.81
	629.14 m Dup	22.8	0.155	0.99	2.57
	630.55 m*	17.8	0.202	41.7	4.03
	820.05 m	3.10	0.134	5.02	5.31
	820.74 m	3.58	0.135	-0.29	0.94
	821.80 m*	3.68	0.254	56.6	4.83
	821.80 m Dup	4.09	0.126	1.76	0.93
	822.41 m	4.94	0.121	2.70	2.99
Spruce Pine Intrusion	IOTA-1	0.70	0.105	4.33	4.70
	IOTA-2*	0.52	0.303	16.6	4.25
	IOTA-3*	0.36	-	8.38	1.48
	IOTA-4	-	-	-	-
Great Artesian Basin	BB2 30.4	2.21	0.049	0.56	-0.48
	BB2 60	9.59	0.027	0.70	2.35
	NB2 35.5*	1.86	0.763	59.8	5.95
	NB2 35.5 Dup	2.25	0.088	1.95	0.92
	NB2 53.4	5.21	0.057	2.09	3.20
	NB2 114	7.72	0.023	0.65	2.99
	NB2 114 fine	8.44	0.022	1.21	2.30
	NB2 114 coarse	3.95	0.033	2.00	-0.83
	NB2 130.5	10.60	0.010	-1.66	0.35
	NB2 149	3.15	0.036	-1.43	2.94
	NB2 176	5.13	0.028	0.68	1.07
	NB2 203	5.15	0.031	1.11	-0.80
	NB2 249	4.94	0.024	1.71	-0.67
	NB2 276.1	4.41	0.031	-1.72	1.00
	NB2 290	5.18	0.033	4.25	2.21

* Helium and helium ratio's presented have been corrected for atmospheric leakage

Formation yielded approximately 10 times more helium than samples of the Lower Kirtland Formation. Samples from the Great Artesian Basin contained 6.21×10^{-8} to 3.97×10^{-7} cc STP He g^{-1} with a median value of 1.92×10^{-7} cc STP He g^{-1}. Initial helium concentrations from Spruce Pine Intrusion were considerably lower with an average concentration of 1.64×10^{-8} cc STP He g^{-1}. It was expected that all samples from the Spruce Pine Intrusion contained the same amount of helium, as they all contain a random distribution of millions of grains. However, variability of 53% was present. This could be attributed to measurement error caused by very low concentrations of helium coupled with error introduced from leak corrections.

Isotherms

San Juan Basin and Spruce Pine Pluton samples were impregnated at multiple pressures to determine the linearity of isotherms. Samples from the San Juan Basin yield an average of $2.3 \pm 0.7 \times 10^{-7}$ cc STP He g^{-1} $Torr^{-1}$ or $4.7 \pm 1.4 \times 10^{-4}$ as a dimensionless He_{quartz}/He_{air} partition ratio. The variation between samples was a factor of 2.4. The maximum partition ratio measured was 8.06×10^{-4} (3.97×10^{-7} cc STP He g^{-1} $Torr^{-1}$) and the minimum was 3.37×10^{-4} (1.66×10^{-7} cc STP He g^{-1} $Torr^{-1}$).

The isotherms of all samples are linear between the pressures measured. Seven of eight samples have R^2 values greater than 0.99 while the remaining sample has an R^2 value of 0.955 (Figure 10). The upper range of impregnation pressures exceed partial pressures of helium that would be found in nature, suggesting that nonlinearity need not be considered when determining pore water helium concentrations from quartz.

Impregnation results from the Spruce Pine Intrusion yields an average partition

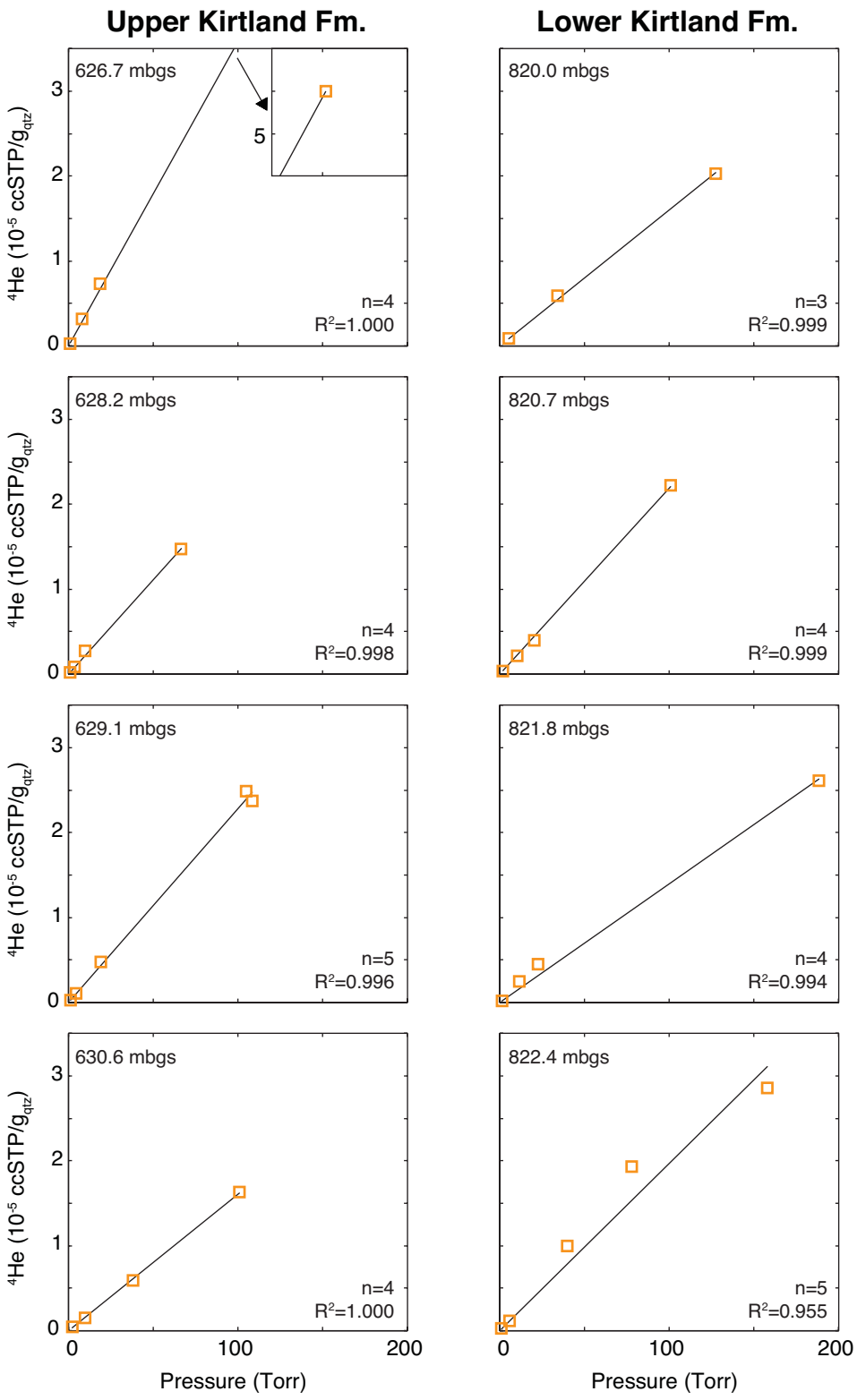

Figure 10: Helium-quartz impregnation results for the Upper and Lower Kirtland Formation

ratio of 6.90×10^{-6} ($3.4 \pm 1.4 \times 10^{-9}$ cc STP He g^{-1} $Torr^{-1}$) or 1.5% of the average measured in San Juan Basin samples. The isotherm is linear but shows a greater amount of scatter (R^2=0.795) between sample fractions and individual impregnations (Figure 11).

Two questions need to be addressed: 1) why is helium uptake significantly lower in Spruce Pine Intrusion samples when compared to San Juan Basin samples, and 2) why is helium uptake not consistent in duplicates of a single Spruce Pine Intrusion sample? The first question is likely attributable to the purity of Spruce Pine samples: When viewed under optical microscope, Spruce Pine samples appear very pure with no mineral or fluid inclusions while San Juan Basin samples contain fluid inclusions among other impurities (Figure 12). Considering the established air-water helium partitioning and the air-quartz helium partitioning presented here, fluid inclusions are likely to contain the majority of helium within a quartz grain. If fluid inclusions are gas filled, it is assumed that at equilibrium the partial pressure of helium within the inclusion is equal to the impregnation pressure. Because helium has an affinity for the gas phase that is approximately 140,000 times greater than quartz, a very small volume of gas is required to explain the discrepancy between San Juan Basin and Spruce Pine samples. Considering San Juan Basin samples and the average ratio of helium released per impregnation pressure, a gas volume of 6.10×10^{-7} cm^3 is required per cm^3 of quartz. This is equivalent to 1.2 million 1 μm diameter spherical inclusions per 1 cm^3. This is a reasonable number considering that milky quartz can contain 10^9 inclusions per 1 cm^3 (Bodnar, 2003; Roedder, 1984). It is unlikely that all fluid inclusions are gas filled in any given sample. However, the phase, composition, and salinity of inclusions are difficult to assess due to the number of grains in each sample. The difficulty is multiplied when

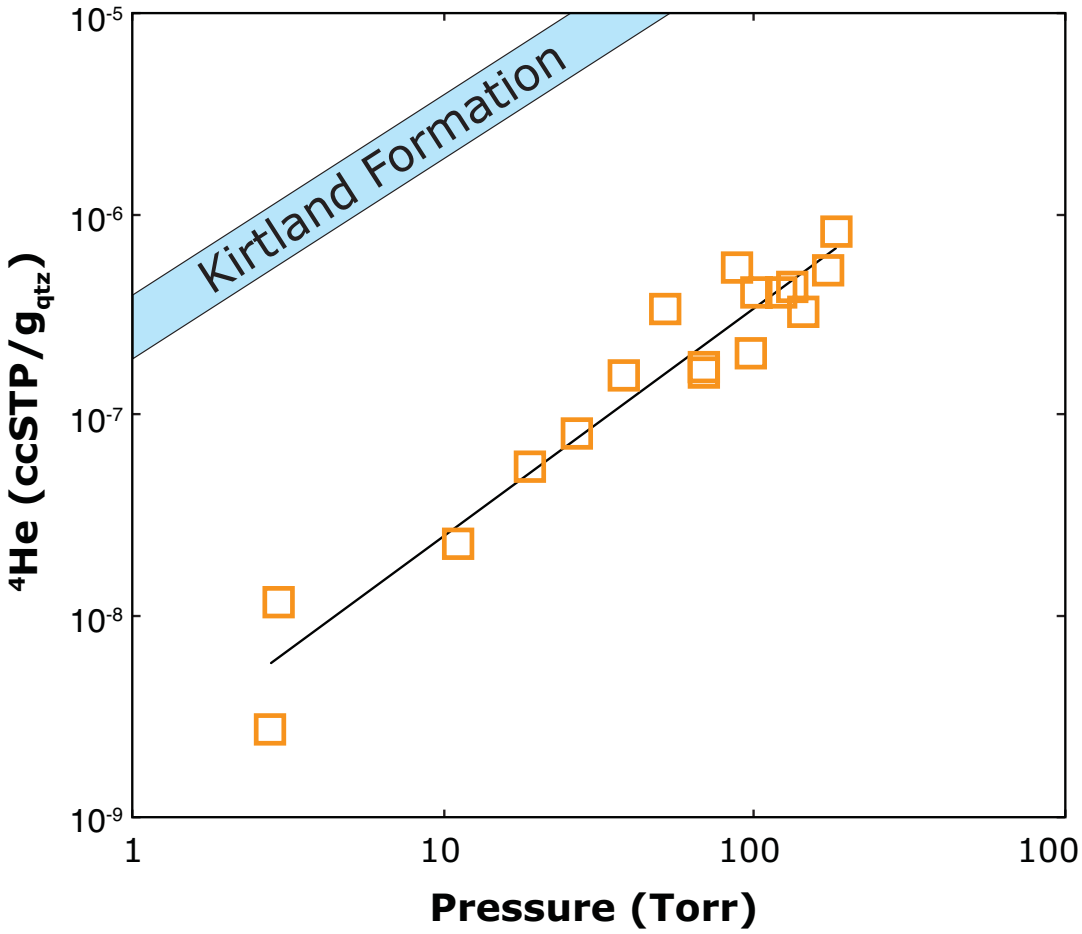

Figure 11: Quartz-air isotherm of helium in Spruce Pine Intrusion samples. Note that Kirtland Formation samples contain approximately two orders of magnitude more helium for a given impregnation pressure.

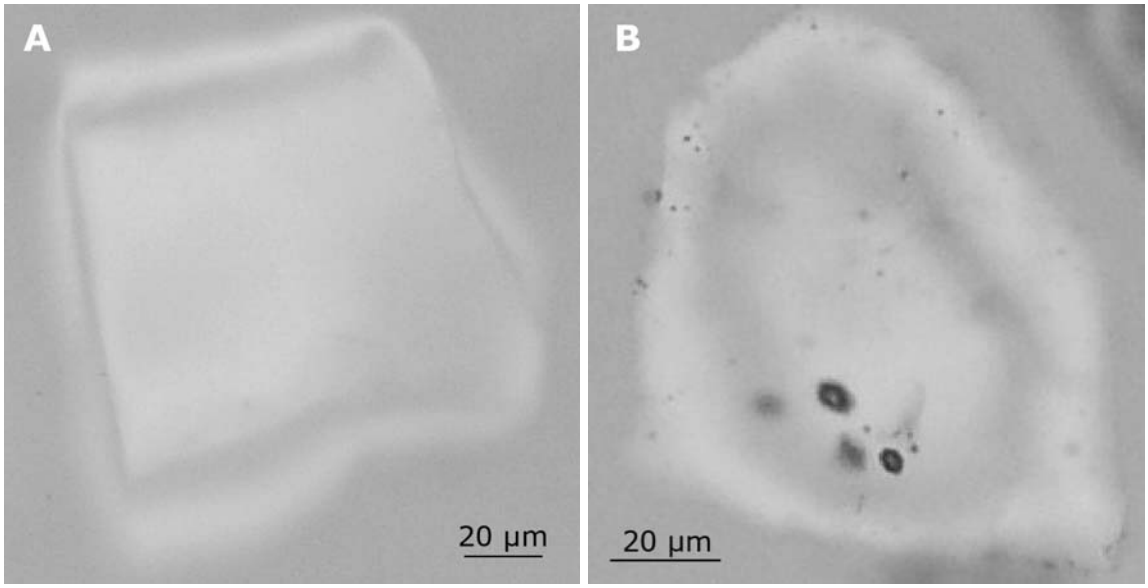

Figure 12: Plane-polarized light photomicrograph of quartz. A) Spruce Pine Intrusion and B) the Upper Kirtland Formation showing fluid inclusions.

considering inability to determine the phases present at 290°C and helium solubility in pressurized, possibly superheated liquid. The second question regarding the scatter of data in the Spruce Pine Intrusion isotherm can be explained by considering the sample size. Figure 11 shows that helium uptake in the Spruce Pines Intrusion samples were significantly lower than San Juan Basin samples and as a clear consequence, the absolute amount of helium introduced to the mass spectrometer was significantly lower. This causes a greater uncertainly in calculating helium concentrations and the uncertainty in corrections adds another source of error. If 100 g (instead of 1 g) of this high purity quartz were impregnated and analyzed, it is expected that the scatter would diminish.

The linearity of isotherms was not determined for Great Artesian Basin samples as they were all impregnated at the same pressure of approximately 21 Torr. The average helium uptake was $4.4\pm0.5\text{x}10^{-7}$ cc STP He g^{-1} $Torr^{-1}$ or 91% greater than San Juan Basin samples.

Pore fluid helium

Pore water helium was determined for San Juan Basin and Great Artesian Basin samples and compared to pore water helium concentrations calculated using the method of Osenbrück et al. (1998). The pore water helium calculation is that of Lehmann et al. (2003). Using the ideal gas law, the helium-accessible volume V_2 (cc STP ^{4}He cm^{-3}) of each quartz sample was determined using:

$$V_2 = V_1 \cdot (P_1/P_2)(T_2/T_1), \tag{8}$$

where V_1 is the measured helium (cc STP ^{4}He cm^{-3}) from impregnation at pressure P_2

(atm) and temperature T_2 (K). P_1 and T_1 are the standard pressure (1 atm) and temperature (273 K), respectively. The He-accessible volume varied between samples and between analyses (Table 2). There was no consistent trend of V_2 increasing or decreasing with either pressure or analysis number. This suggests that fluid inclusions and crystal defects within a given sample were not irreversibly changed through each analysis (Figure 13). The He-accessible volume was an average of $1.8\pm0.2\text{x}10^{-3}$, $1.0\pm0.3\text{x}10^{-3}$, and $1.4\pm0.6\text{x}10^{-5}$ cc STP He cm^{-3} for the Great Artesian Basin, San Juan Basin, and Spruce Pine Intrusion, respectively. In other words 0.18%, 0.10%, and 0.0014% of the quartz volume was available to the helium. The helium-accessible volumes of the Great Artesian and San Juan Basins are similar to those measured by Lehmann's work in the Permo-Carboniferous Trough in Northern Switzerland at 0.018% to 0.13% (2003).

With the air-water solubility of helium S (cc STP He g_w^{-1} atm^{-1}), the initial helium released from the quartz c_{ini} (cc STP He cm^{-3}), and the *in situ* formation temperature T_f (K), the pore water concentration may be calculated using

$$c_w = S(c_{ini}/V_2)\left(T_f/T_1\right). \tag{9}$$

This equation assumes that in a three-phase system of air, water, and quartz, helium is partitioned to equilibrium between the three-phases. Pore water concentrations for the San Juan Basin are distinctly different in the Lower and Upper Kirtland Formation (Table 2). The four samples of the Lower Kirtland Formation contain between 3.9 and $5.2\text{x}10^{-6}$ cc STP He g_w^{-1}, which is 84-113 times greater than atmospheric solubility. Previous helium measurements (Heath, 2010) in the Lower Kirtland Formation were between 2.2

Table 2: He impregnation and pore water He results

	Sample	Impregnation Pressure (Torr)	^{4}He cc STP cm^{-3} (x10^{-7})	He-accessible volume cc STP cm^{-3} (x10^{-4})	Pore water He cc STP cm^{-3} (x10^{-5})
San Juan Basin	626.70 m	154	1472	15.0	5.32
		18.429	196	16.7	4.77
		7.798	84.4	17.0	4.27
		0.942	10.7	17.7	4.08
	626.70 m Dup	21	217	16.3	4.77
		2.615	23.9	14.3	5.41
	628.22 m	67	393	9.25	2.62
		9.807	73.2	11.7	2.07
		0.955	6.65	10.9	2.02
		3.629	25.3	10.9	2.02
	629.14 m	18.961	128	10.6	1.95
		4.595	29.4	10.0	2.06
		1.212	7.66	9.91	1.89
		105	665	9.96	1.88
		108	633	9.15	2.24
	629.14 m Dup	18.414	62.5	5.32	4.48
		4.205	28.4	10.6	2.25
	630.55 m	38	157	6.48	2.87
		9.643	39.5	6.42	2.90
		2.185	11.5	8.21	2.06
		101	435	6.77	2.50
	820.05 m	34	158	7.25	0.45
		5.324	23.6	6.96	0.47
		127	542	6.67	0.44
	820.74 m	21	106	8.07	0.47
		1.934	9.00	7.29	0.52
		101	593	9.22	0.37
		10.216	56.7	8.69	0.39
	821.80 m	188	697	5.80	0.67
		11.347	65.4	9.04	0.43
		23	119.6	8.21	0.43
		1.194	6.11	8.02	0.44
	821.80 m Dup	18.103	109	9.45	0.46
		3.028	17.1	8.87	0.49
	822.41 m	5.797	34.5	9.32	0.56
		158	764	7.59	0.69
		40	267	10.5	0.45
		0.970	6.81	11.0	0.43
		78	516	10.4	0.45

Table 2 Continued

	Sample	Impregnation Pressure (Torr)	^{4}He cc STP cm^{-3} (x10^{-7})	He-accessible volume cc STP cm^{-3} (x10^{-4})	Pore water He cc STP cm^{-3} (x10^{-5})
Spruce Pine Intrusion	IOTA-1	2.783	0.0731	0.04	13.33
		27	2.16	0.13	4.31
		68	4.35	0.10	5.51
		122	10.8	0.14	3.93
		101	10.9	0.17	3.25
	IOTA-2	2.961	0.310	0.16	3.35
		97	7.02	0.11	4.84
		38	4.25	0.17	3.14
		183	22.0	0.19	2.91
	IOTA-3	11.211	0.605	0.08	6.48
		133	11.6	0.14	4.01
		51	8.99	0.27	2.00
		87	14.3	0.26	2.15
	IOTA-4	143	8.68	0.10	5.76
		68	4.62	0.11	5.19
		18.958	1.47	0.12	4.52
		173	14.0	0.13	4.33
Great Artesian Basin	BB2 30.4	20	253	20.0	0.12
	BB2 60	18.651	201	16.9	0.64
	NB2 35.5	21	246	18.4	0.11
	NB2 35.5 Dup	18.541	202	17.0	0.15
	NB2 53.4	25	264	16.7	0.35
	NB2 114	21	242	18.1	0.48
	NB2 114 fine	18.784	214	17.9	0.92
	NB2 114 coarse	19.471	296	23.9	0.19
	NB2 130.5	21	243	18.3	0.65
	NB2 149	21	247	18.5	0.19
	NB2 176	23	275	18.9	0.31
	NB2 249	23	331	22.7	0.24
	NB2 276.1	20.300	230	17.7	0.28
	NB2 290	17.647	178	15.8	0.37

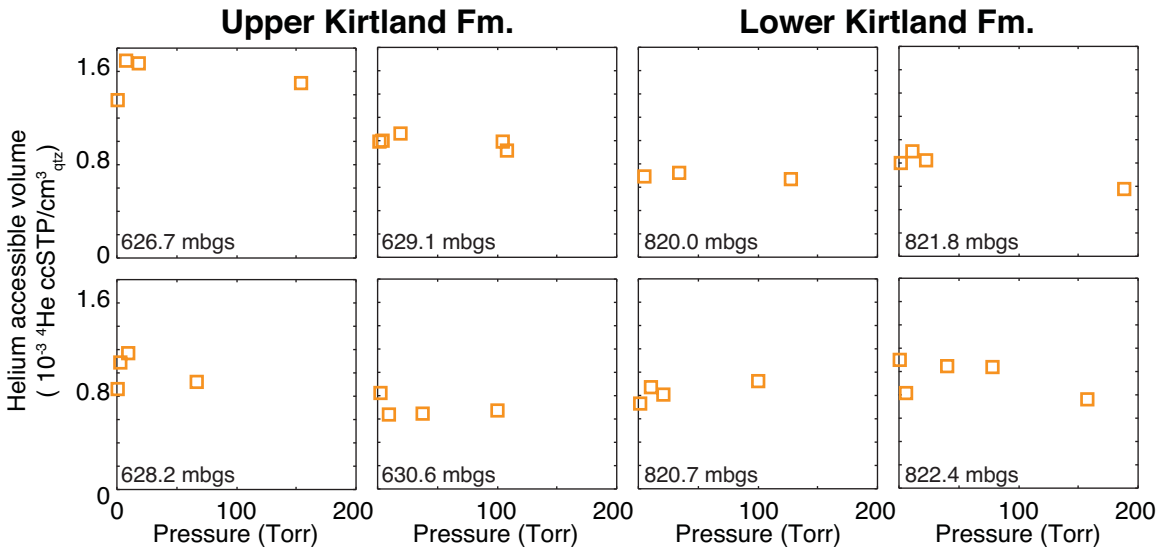

Figure 13: Helium-accessible volume calculated for San Juan Basin samples.

and 5.4×10^{-5} cc STP He per pore volume. Given average U and Th concentrations measured in the Kirtland Formation yield a helium production rate of 1.78×10^{-11} cc STP He g_w^{-1} yr^{-1}, 0.3 to 0.4% of the produced radiogenic helium remains in the Lower Kirtland Formation. The pore water helium concentrations in the Upper Kirtland were between 2.2 and 4.8×10^{-5}, or 1.7 to 3.7% of radiogenic helium produced since deposition 73.05 Ma. Previous helium measurements (Heath, 2010) in the Upper Kirtland Formation were between 0.7 and 1.2×10^{-4} cc STP He per pore volume.

The mineral-fluid He partition ratio K_d in Kirtland Formation samples is

$$K_d = C_m / C_f, \tag{10}$$

where C_m and C_f are the equilibrium mineral phase and fluid phase concentrations, respectively. The mean value was $\sim 10^{-1}$, whereas Spruce Pine Intrusion samples have K_d values of $\sim 10^{-3}$. The latter value corresponds with estimates for He and Ar (Brooker et al., 1998). The K_d value for the Kirtland Formation is significant, indicating that if equilibrium occurred between quartz and pore water found in a quartz sandstone with 10% porosity, equal amounts of helium would be found in the quartz as the pore water per volume. This is a very significant sink for radiogenic helium.

With the exception of one sample in the Upper Kirtland Formation, all pore water helium concentrations are 21-91% less than the measurements of Heath (2010) with the biggest difference in the Lower Kirtland Formation. At this point it is difficult to determine which measurements were more accurate. The canister method, when done properly has the potential to lose 20-30% of dissolved noble gases (Osenbrück et al.,

1998) but if that were the case we would expect less helium in Heath's (2010) analysis. Another potential problem with the canister method is accounting for unsaturated conditions due to methane or carbon dioxide production at depth. A gas phase was detected in the Upper Kirtland using an ELAN log (Heath, 2010) however, a gas phase was not detected in the Lower Kirtland where the greatest discrepancy is present. In addition core analysis (Terra Tek) showed a gas phase occupying 11-24% of the pore space. But, this gas may have been introduced by methane exsolving when the samples were depressurized (Heath, 2010). Regardless of whether the ELAN log or core analysis is correct, at a depth of 800 m and assuming hydrostatic pressure, if 1% of the pore volume was unsaturated, the total helium in gas phase would exceed the total dissolved helium and if the pore volume was 8% unsaturated, the total helium in the gas phase would comprise 90% of the total helium.

To complicate the matter, there are two alternate explanations for the lower-than-expected pore water helium concentrations determined from quartz analysis: 1) equilibrium partitioning of helium between quartz and water was not present at the time of sampling or 2) helium was lost during processing including crushing and heating. Assuming that the diffusivity of helium in quartz is correct, at 35°C the degree of equilibrium between a 150 μm spherical quartz grain and water should exceed 99.9% after 73 My. If the diffusivity were an order of magnitude lower, the degree of equilibrium would still exceed 99%. It is possible that the hydraulic conditions have varied over time and equilibrium was not reached, however, this issue is beyond the scope of this study.

The possibility of helium loss during processing may be a more real problem. The

breaking of quartz grains during mineral separation would cause a loss of helium (Ballentine and Burnard, 2002). However, the determination of the helium-accessible volume would correct for this issue as broken fluid inclusions would produce a lower helium-accessible volume, resulting in a larger pore water concentration (see Eqn. 9). Heating samples for drying purposes could cause a loss of helium if the diffusivity was significantly higher than values of Trull et al. (1991). Helium diffusivity was measured by Shuster and Farley (2005) who produced ^{3}He and ^{4}He by proton bombardment in inclusion-free quartz. The resulting diffusivity at 25°C is five orders of magnitude higher than Trull et al. (1991) measured, suggesting that significant amount of helium would be lost at ambient temperature. However, if this diffusivity represented Kirtland Formation samples, virtually all helium would be lost between the time of coring in May 2008 and when this project commenced in the fall of 2010. This suggests that helium is retained in fluid inclusions but may be lost from the crystal lattice and is supported by other literature (Cerling, 1990; Niedermann, 2002). Comparing San Juan Basin and Spruce Pine Intrusion and implying this dual diffusivity model, helium lost from the crystal lattice comprises of only ~1.5% of the total helium. This loss combined with potential loss from heating at 60°C for the purpose of sample drying yields a total loss of ~2%. If diffusivity were 10x larger, the total loss is ~3%. Unless ambient temperature diffusivity is significantly greater than the results of Trull et al. (1991), this offset cannot be definitively resolved. The presence of a gas phase in Heath's analysis or helium loss through heating in this study could produce the results we see but we cannot separate the two with the present data. Even if some helium was lost through processing, these measurements show that a significant amount of helium was contained in the Kirtland

Formation, suggesting significantly low fluid flux rates.

Pore water concentrations in the Great Artesian Basin are between 1.0 and 6.5×10^{-6} cc STP He g^{-1} and the pore water helium concentration does not change appreciably with depth as seen in samples collected using the canister method (Figure 14). As suggested with the San Juan Basin samples it is possible that these samples could have some degree of degassing through heating involved in mineral separation. However, the diffusivity does not agree with this explanation. Another possibility is that equilibrium of helium between pore water and quartz was not reached. To address this idea, it is possible to see if more helium can be found in smaller grains or larger quartz grains. If more helium is found in larger grains relative to smaller grains, this suggests that helium is lost through heating during processing as the smaller grains equilibrate more rapidly. The opposite condition (more helium in smaller grains) could mean *in situ* quartz-pore water equilibration never occurred. Quartz from 114 m depth in Nancy's Bore was separated into two fractions: 44-90 μm and 91-150 μm. Both fractions were evacuated of atmosphere as described above and heated for 10 days. The fine-grained fraction released 3.16×10^{-7} cc STP He g^{-1} and the coarse grained fraction released 1.48×10^{-7} cc STP He g^{-1} or 47% released from the fine-grained sample. This information alone suggests two possible causes: 1) helium equilibrium between pore water and quartz did not occur or 2) helium was not being completely released during the 10 days of heating at 290°C. Further testing of helium release from different size fractions could provide insight into the degree of equilibrium; however, this is outside the scope of this study.

It is possible that helium was not reaching equilibrium between quartz and pore water in the calculated times. This may not be traced to laboratory diffusion experiments

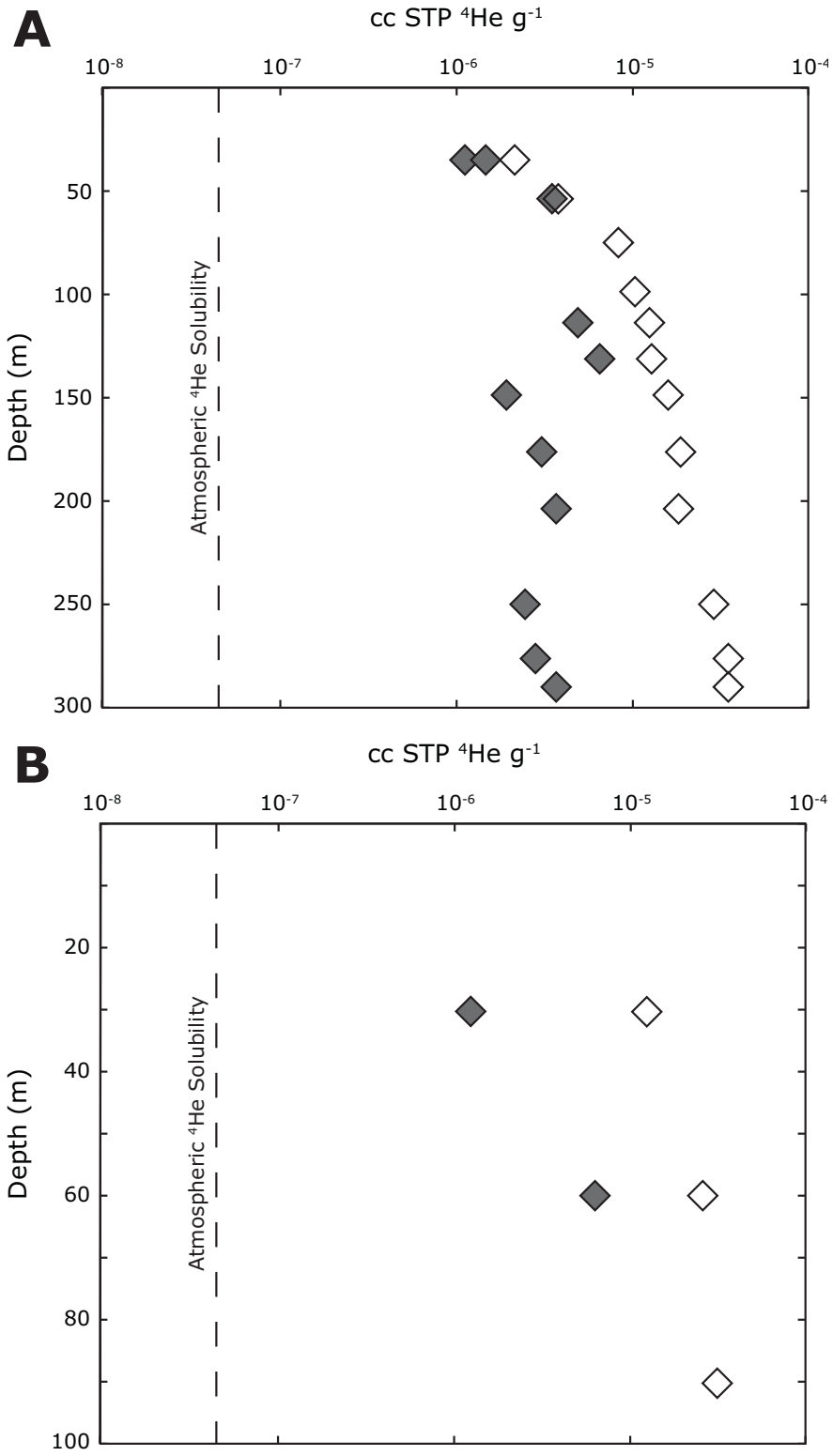

Figure 14: Great Artesian Basin pore water concentrations. Filled diamonds=quartz method, open diamonds=canister method (Gardner et al., submitted). A) Nancy's Bore and B) Birthday Bore.

but instead to the spatial distribution of quartz relative to pore water within the rock matrix. If quartz was isolated from pore fluids, the diffusion pathways could be limited, preventing helium from diffusing into the quartz grain at its entire surface area. Alternatively, if quartz grains are completely coated by clay or other mineral phases, helium would need to diffuse through the coating before diffusing into the quartz; possibly increasing the effective diffusion time by orders of magnitude. This issue cannot be quantitatively assessed at this point because the diffusivity of helium through minerals, excluding U-bearing minerals, has received little attention and data are sparse (Baxter, 2010).

Helium modeling

The spatial and temporal distribution of helium was simulated using a general 2-D model with a low-permeability zone and a site-specific 1-D model for the Kirtland Formation of the San Juan Basin.

The distribution of radiogenic helium in a hypothetical basin was determined using 2-D finite-volume advection-diffusion modeling. A qualitative basin-scale model was based on the modeling results of Stute et al. (1992), who modeled 2-D steady-state groundwater flow (Tóth, 1963) with the addition of helium production. The model presented here was developed using TOUGH2, a nonisothermal multiphase flow simulator (Pruess et al., 1999). The equation of state EOS7R (Oldenburg and Pruess, 1995) was used for its ability to simulate transport of low-concentration tracers within aqueous and gas phases. The cross-sectional model grid dimensions are X=5,000 m, Y=10 m, and Z=1,000 m. Grid blocks are equally sized at 50 x 10 x 10 meters (XYZ).

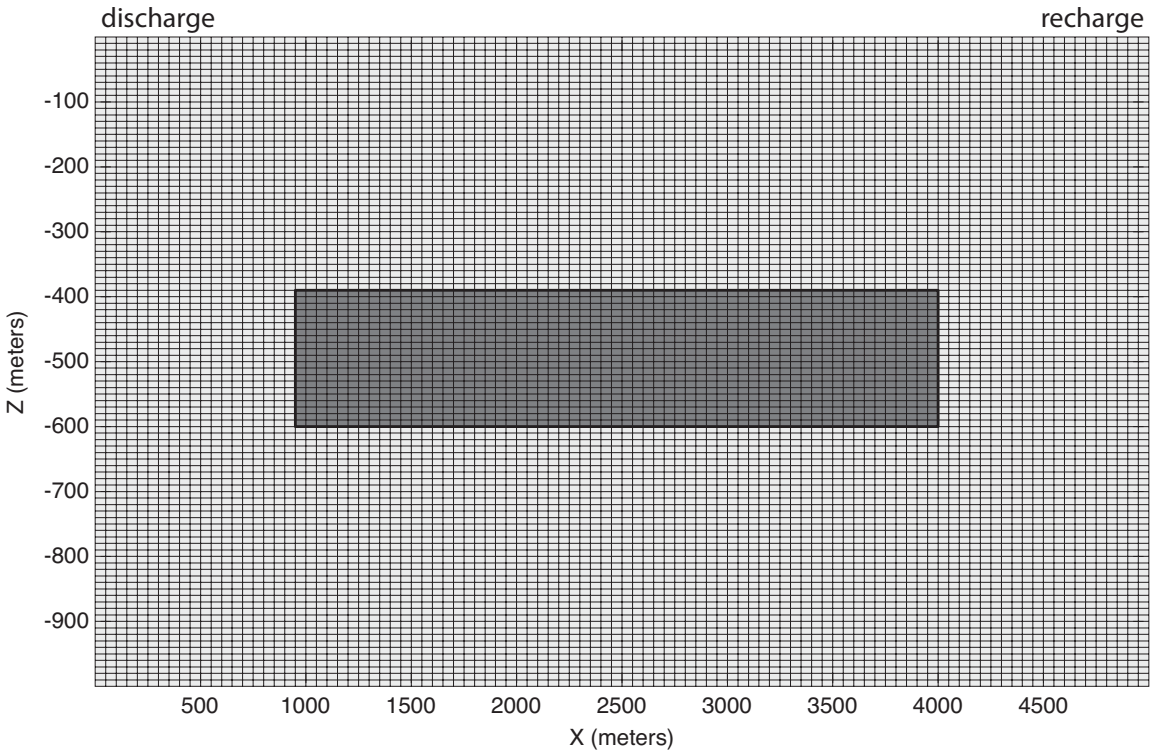

Figure 15: TOUGH2 model domain. Centered in the model is the low permeability lens, which is surrounded by the aquifer.

The simple and generalized model was split into two domains: a relatively high permeability sandstone zone (herein referred to as the aquifer) and a centered shale lens 3,000 m wide and 200 m thick with a lower permeability (Figure 15). The horizontal to vertical permeability ratio (k_h/k_v) was 10 throughout the model domain. The k_h of the aquifer was 10^{-15} m^2 and the k_h of the shale lens was varied between 10^{-15} to 10^{-20} m^2 in order of magnitude steps. The right, left, and bottom boundaries were impermeable to flow. The upper boundary had a constant head that decreases linearly in the negative X direction producing a gradient of 0.01 to maintain groundwater flow. Before modeling the helium distribution, the model was run to steady state to obtain a head distribution as an initial condition to the helium model (Figure 16). This baseline step prevents attribution of erroneous helium concentrations to transient flow conditions.

Helium may exit the model through the upper boundary, simulating loss to the atmosphere. As this model only considers radiogenic helium, atmospheric solubility of helium was not considered because its contribution is small relative to radiogenic production. The lower boundary was simulated as impermeable to helium. Helium was produced within the domain at a constant rate of 5.64×10^{-20} kg s^{-1} m^{-3} (Stute et al., 1992). The effective porosities n of the sandstone aquifer and shale lens are 0.2 and 0.005, respectively (Schwartz and Zhang, 2003). It was assumed that in the aquifer, the effective porosity was equal to the total porosity and that the total porosity in the lens was 0.10. At steady state it was assumed that helium in the immobile pore fluids would have the same helium concentration as mobile pore fluid. This is comparable to introducing a reversible linear adsorption factor to the lens porous media. Considering the total porosity of 0.10 and effective porosity of 0.005 (maximum range; Schwartz and Zhang, 2003), 95% of the

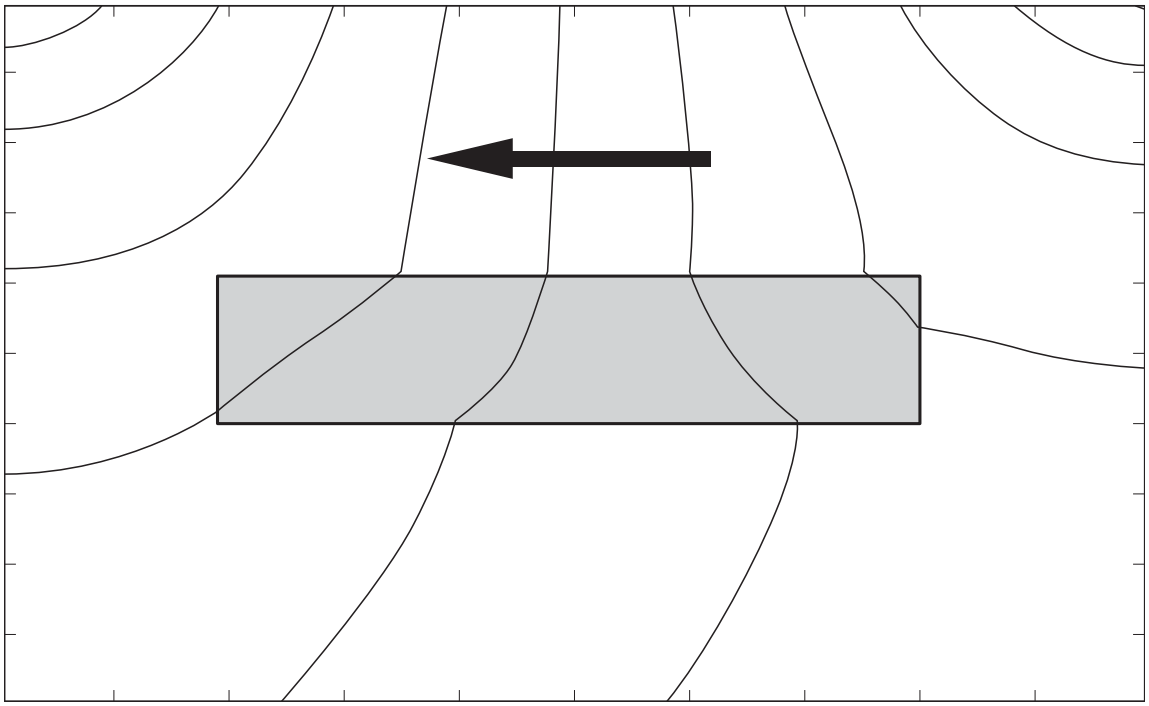

Figure 16: Steady-state hydraulic head distribution with lens $k_h=10^{-18}$ m^2. Contour interval is 5 m.

total porosity was immobile and contains 95% of the helium per unit volume. A K_d value of 4×10^{-5} m^3 kg^{-1} was used to simulate the dual porosity effects as determined by the mass balance output of TOUGH2. Furthermore, the steady-state distribution of helium was unchanged from the model that does not consider adsorption. The effective diffusivity D_e of helium is calculated by TOUGH2 using the equation (Pruess et al., 1999):

$$D_e = n\tau_o\tau_\beta D_\beta, \tag{11}$$

where $\tau_o\tau_\beta$ is the tortuosity factor of solute β in porous media o. This value includes a porous media factor τ_o and the saturation dependent factor τ_β. Because the model always contains a single phase, τ_β is assumed to equal one. D_β is the free solution diffusion coefficient of helium in water: 6.3×10^{-9} m^2 s^{-1} (Jahne et al., 1987). The tortuosity is calculated using the approximation (Schwartz and Zhang, 2003):

$$\tau_o = n^{1/3}, \tag{12}$$

which yields tortuosity factors of 0.58 and 0.17 for the aquifer and lens, respectively. The effective diffusivities calculated using Eqn. 11 are 7.3×10^{-10} m^2 s^{-1} for the aquifer and 5.4×10^{-12} m^2 s^{-1} for the shale lens.

The simulations were run until the helium distribution reached steady state, which occurred within 5-10 million years. The model results show that helium was retained within the shale lens due to the lower permeability. The mean helium concentration

within the lens increases from 6.25×10^{-7} cc STP He g^{-1} when $k_h=10^{-15}$ m^2 to 1.20×10^{-5} cc STP He g^{-1} when $k_h=10^{-20}$ m^2. It is notable that the concentration of helium in the lens was not appreciably affected by the magnitude of permeability below 10^{-18} m^2 (Figure 17, Figure 18). This suggests that below a critical fluid velocity, diffusion is the dominant transport mechanism.

After 15 million years, the percent of produced helium was calculated and shows that a maximum of over 23% of the produced helium was retained in the center of the lens when the permeability was less than or equal to 10^{-8} m^{-2} (Figure 18). In comparison a mean value of 2.5% was found in the high permeability zone. In a real sedimentary basin, the helium concentration contrast between the shale lens and sandstone aquifer is likely to be increased due to a general lack of U and Th in sandstone (Heath, 2010; Tolstikhin et al., 2005).

Considering the $k_h=10^{-18}$ m^2 model, the mean fluid velocity through the lens was 1.38×10^{-6} m day^{-1} suggesting that the residence time of fluid in the lens is on the order of six million years. However, the water residence time may be calculated using

$$t = \frac{^4\mathrm{He}_r}{J_{\mathrm{He}}}, \tag{14}$$

where t is the water residence time and J_{He} is the helium accumulation rate (Kipfer et al., 2002). Using Eqn. 14 and the mean helium concentration of 1.16×10^{-5} cc STP He g^{-1}, the He residence time is approximately 2.3 million years. Both estimates are significantly large when considering the permeability of caprock appropriate for indefinite storage of CO_2.

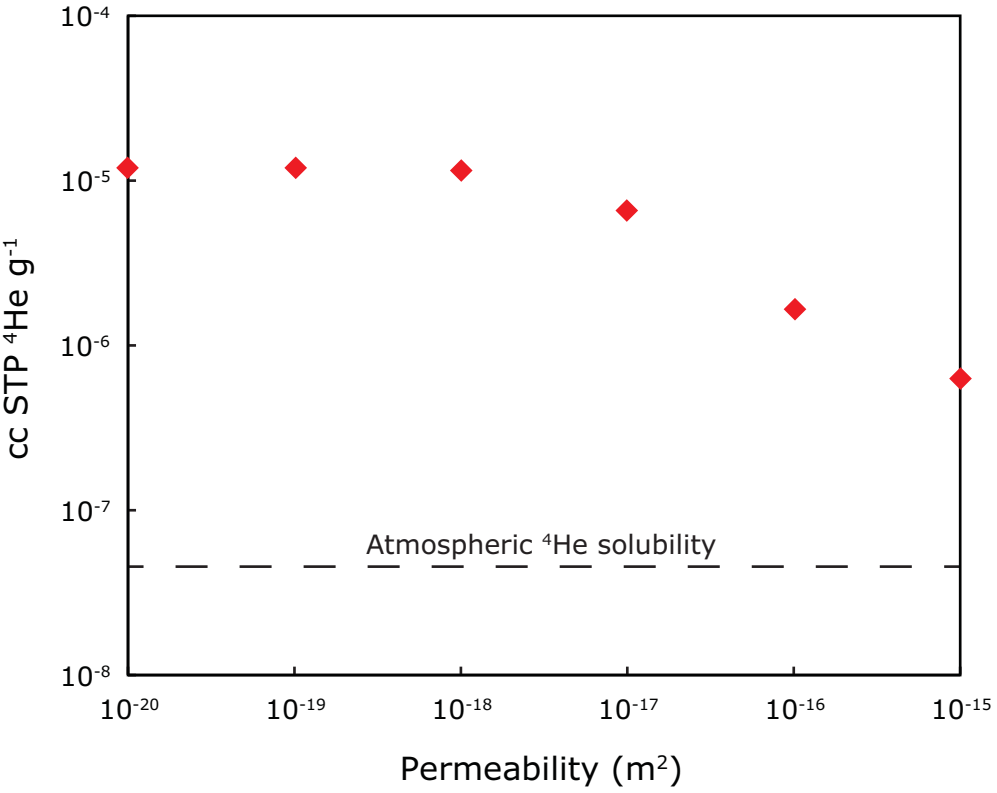

Figure 17: Average helium concentration in the low permeability lens as a function of lens permeability.

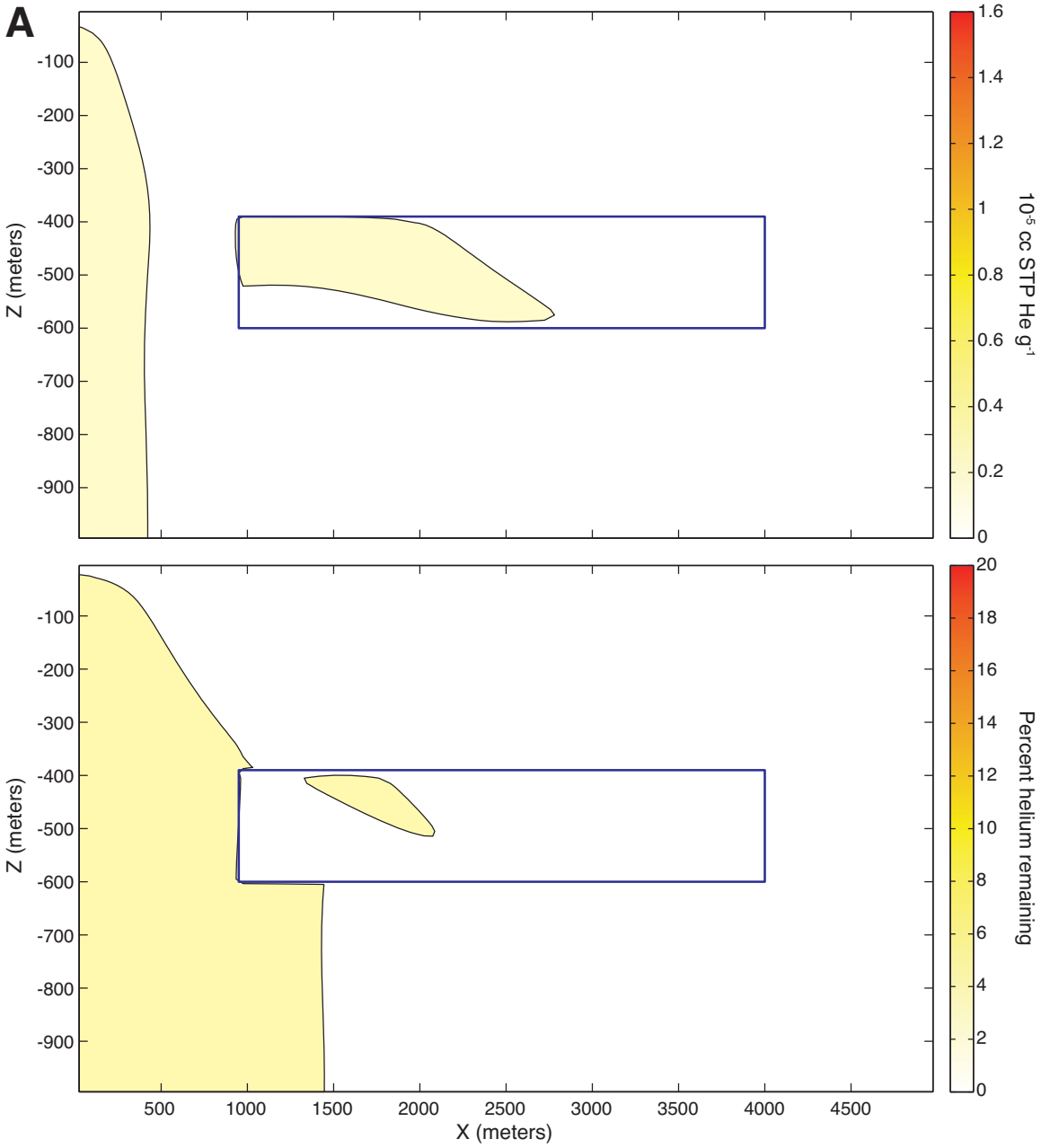

Figure 18: Helium modeling results. Lens horizontal permeabilities are A) 10^{-16} m^2 B) 10^{-18} m^{-2} C) 10^{-20} m^2. The contour interval is $0.2x10^{-5}$cc STP He g^{-1} for concentration plots and 4% for helium remaining plots. Note that the presence of elevated helium concentrations on the left side of the model domain are caused by longer flow paths, which increase the residence time and allow a greater accumulation of radiogenic helium. The abrupt change in percent helium remaining is caused by the dual porosity within the low permeability lens.

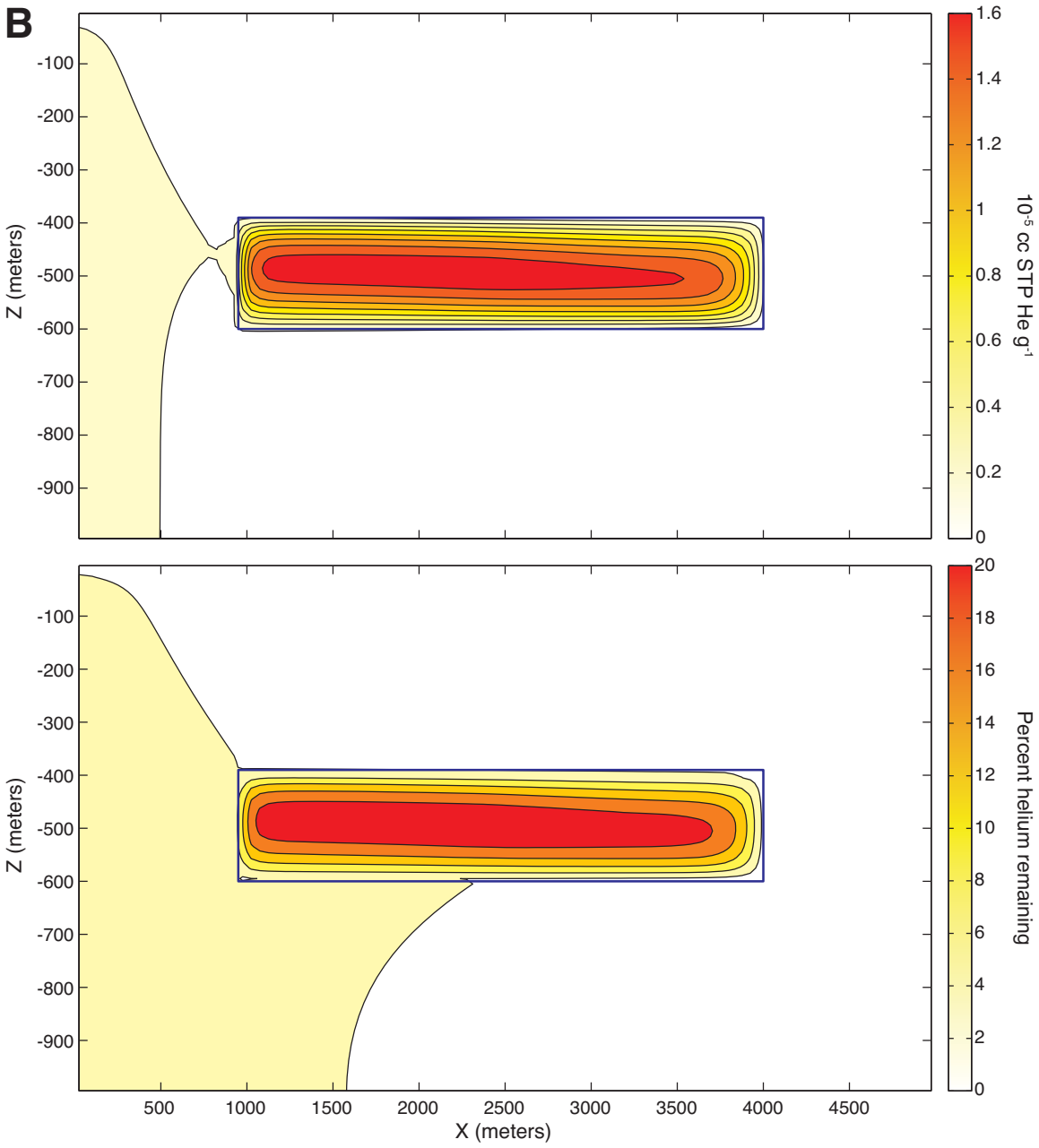

Figure 18 Continued

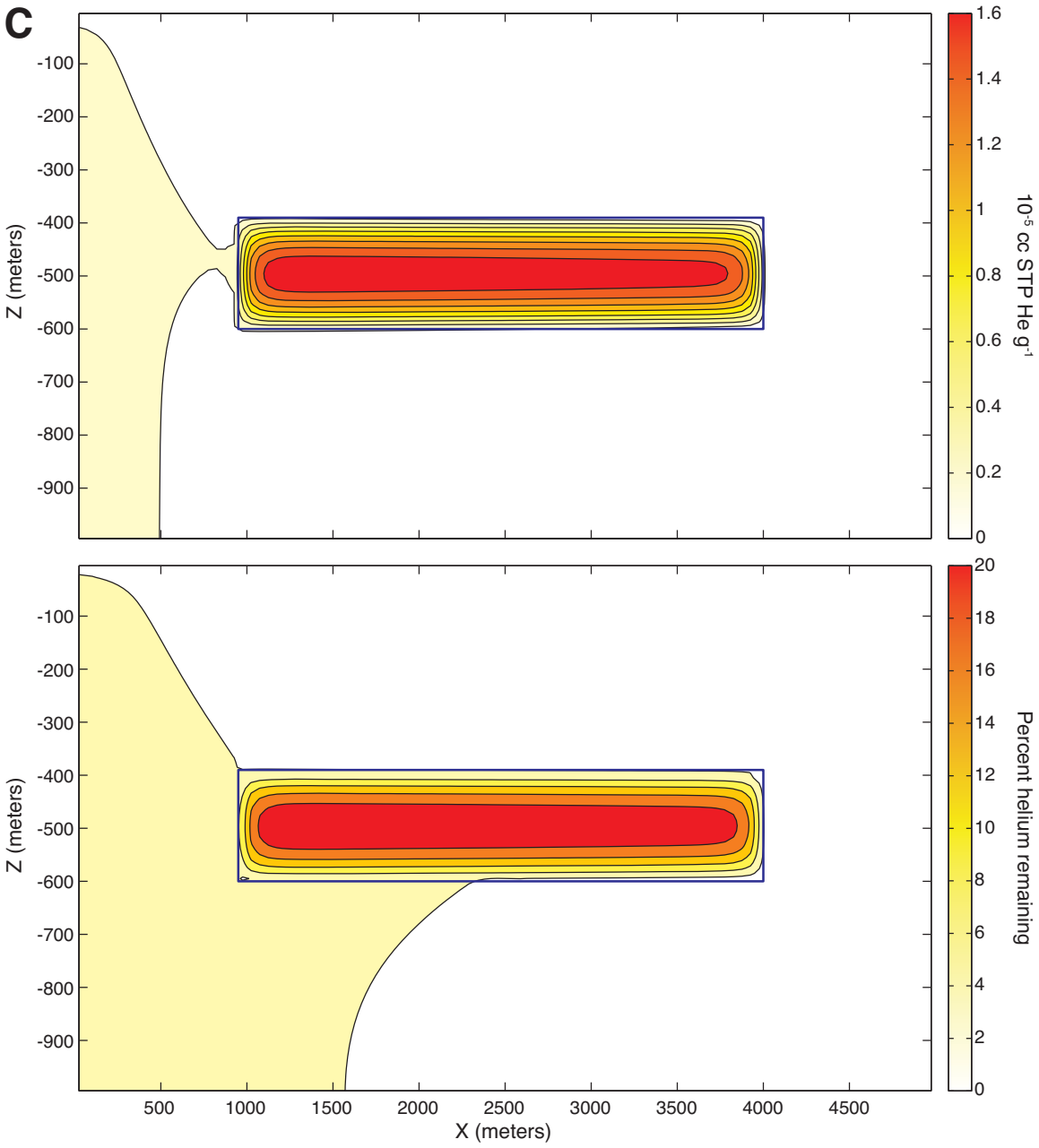

Figure 18 Continued

A fracture zone in the low permeability lens was added to determine the spatial effect on helium concentrations. The 50 m wide fracture zone was simulated by increasing the permeability. The bulk permeability of fracture zone was determine using the equivalent continuum approach (Schwartz and Zhang, 2003):

$$k = \frac{k_m + \frac{A_f}{A_m} k_f}{1 + \frac{A_f}{A_m}}, \tag{15}$$

where k is this bulk permeability, k_m is the matrix permeability (10^{-18} m^2), k_f is the fracture permeability, and A_f and A_m are the cross-sectional area of the fractures and matrix, respectively. If fractures have 0.5 mm apertures, k_f is 2×10^{-8} m^2 using the cubic law (Romm, 1966), and the ratio between fracture and matrix cross-sectional area is 5×10^{-8}, the bulk permeability is 10^{-15} m^2. This is a conservative estimate and permeability could be orders of magnitude larger if fracturing were more extensive.

After running the model to steady state, helium concentrations within the fracture zone are up to 88% lower than the reference model and the helium concentrations within the unfractured lens have decreased up to 10% in the zone 250 m adjacent to the fracture zone and 50% in the zone 50 m adjacent to the fracture zone (Figure 19). It is notable that helium concentrations are elevated above the fracture zone as helium diffusing from the fracture zone was advected into a plume. This suggests that dissolved helium concentrations could be sampled at the top of the low permeability zone using more conventional dissolved gas collection techniques, and anomalously high helium concentrations could indicate a fracture zone.

Overall, helium was retained in low-permeability layers relative to surrounding

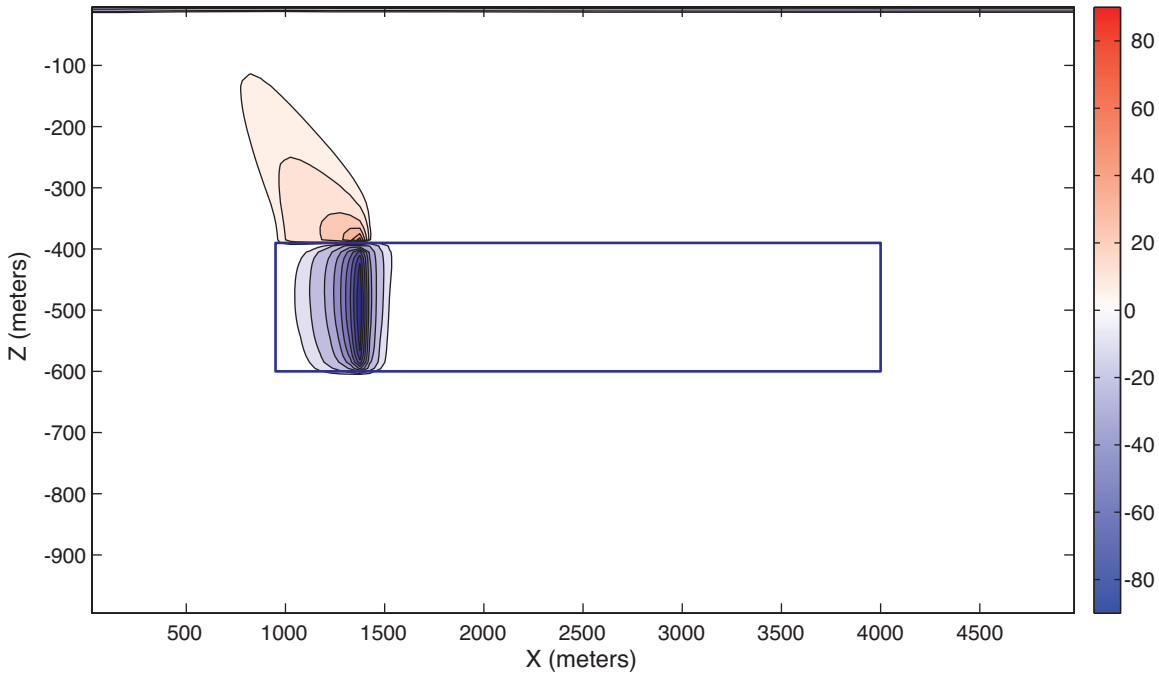

Figure 19: Perturbation in helium distribution due to fracture zone. Contour interval is 10% with the addition of the -5% and 5% level.

high permeability layers. In the geometry modeled here, permeabilities below 10^{-18} m^2 have little effect on helium retention as diffusion was the dominant cause of helium loss and advection has little effect. One limitation of this model was that it assumes groundwater has a high fluid flux in the aquifer below the caprock. If flow were limited within the saline aquifer, helium concentrations may approach those seen in the caprock and high helium concentrations would be less evident of low permeability. This issue and others related to realistic basins are considered below.

With the helium data present and hydraulic conditions at the Pump Canyon site, the bulk permeability of the Kirtland Formation was determined using one-dimensional advection-diffusion modeling. The methods used follow those of Heath (2010) who assumes a steady-state system with a purely vertical hydraulic gradient. The analytical solution to the advection-diffusion equation with uniform internal production of helium:

$$c(z) = \left(c_l - \frac{gL}{V_z}\right)\frac{\left(1-\exp(zV_z/D)\right)}{\left(1-\exp(LV_z/D)\right)} + c_u\left(\frac{\exp(zV_z/D)-\exp(LV_z/D)}{1-\exp(LV_z/D)}\right) + \frac{gz}{V_z}, \quad (16)$$

where $c(z)$ is the helium concentration in the pore water at depth z, c_l and c_u are the helium concentrations at the lower and upper boundaries, respectively, g is the helium production rate and was based on measured U and Th concentrations (Heath, 2010), L is the thickness of the Kirtland Formation, and V_z is the vertical fluid velocity. The lower boundary concentration was determined from the solubility of helium in water and helium concentrations measured in gas samples from the underlying Fruitland Formation (Zhou and Ballentine, 2006). The upper boundary was considered to be one of zero gradient as the hydraulic gradient is vertical at this site suggesting that helium is not

being immediately transported via advection as it exits the Kirtland Formation. Helium diffusivity was calculated using Eqn. 11 and the measured range of porosities (Heath, 2010). It was assumed that the saturation dependent factor τ_β equals one even though core analysis and well logging suggest two phases are present within the Kirtland Formation (Heath, 2010). Regardless, the plausible range of diffusivities in the Kirtland Formation has little effect on the resulting helium distribution. All model parameters are presented in Table 3. The pore water helium data were best fit to the model by modifying the production rate, within the range supported by U and Th concentrations, the vertical fluid velocity, and the lower boundary condition (Figure 20). The permeability of the Kirtland Formation was determined using Darcy's Law, thus assuming that the porous media was fully saturated even though that may be an oversimplification as noted above.

Table 3: Kirtland Formation 1-D advection-diffusion model parameters.

Parameter	Value Range	Units
D	0.005-0.008	$m^2\ yr^{-1}$
g	$0.81\text{-}2.65 \times 10^{-11}$	cc STP He $g^{-1}\ yr^{-1}$
c_l	$0.03\text{-}5.86 \times 10^{-6}$	cc STP He g^{-1}
c_u	variable	cc STP He g^{-1}
V_z	variable	$m\ yr^{-1}$
L	240	m
∇h	0.6-1.2	$m\ m^{-1}$

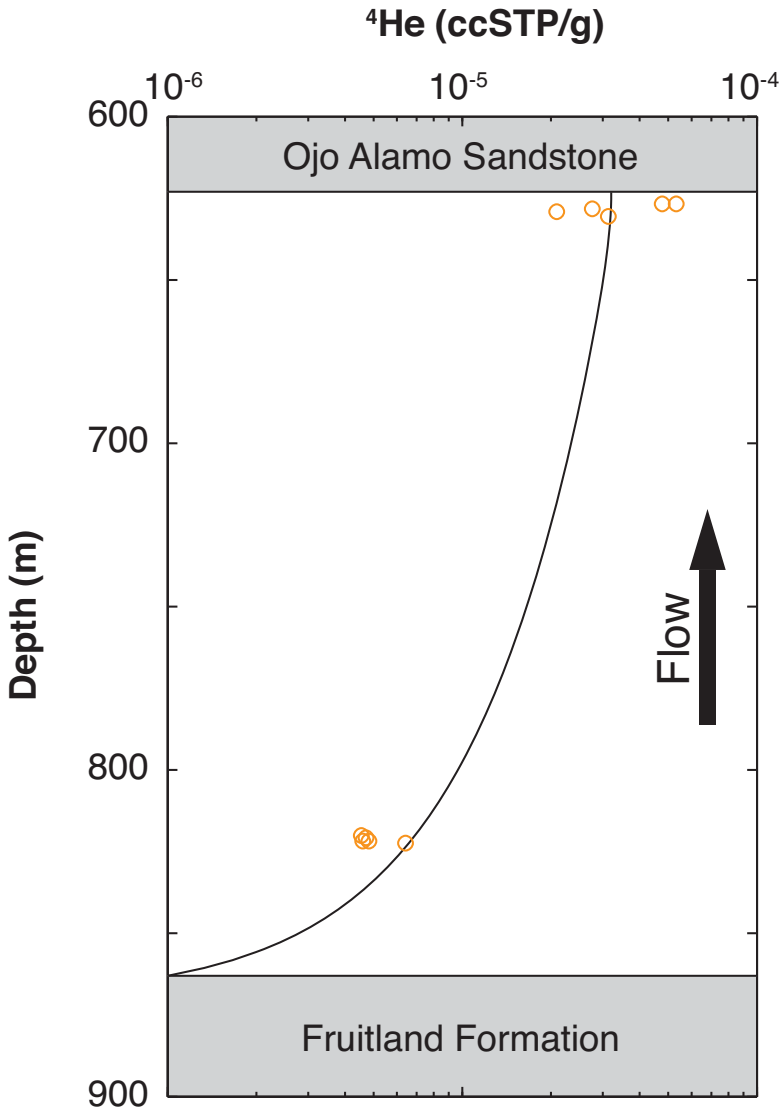

Figure 20: 1-D advection dispersion results for the Kirtland Formation

By fixing the lower boundary concentrations at 10^{-6} cc STP He g^{-1}, and allowing the helium production rate to vary within the measured range, the velocity which best fits the data, ranges between $6x10^{-5}$ and $2x10^{-4}$ m yr^{-1}. With a porosity of 0.10, and the modeled vertical hydraulic gradient, the permeability of the Kirtland Formation is between $6.5x10^{-20}$ and $1.1x10^{-19}$ m^2, which is on the same order as Heath's (2010) results which used different boundary conditions and different helium concentrations. This indicates that regardless of the order of magnitude differences seen in this study and Heath's results, the Kirtland Formation has a very low permeability. It should be noted that the spatial distribution of samples is very limited and when considering the 240 m thick Kirtland Formation as a whole, the eight available data points essentially consist of two points. With the available data, it is impossible to rule out the presence of a seal bypass system, as the majority of the model domain is unconstrained by helium concentrations. Future studies should focus on taking samples throughout the thickness of the caprock and at the boundaries in order to better constrain the boundary conditions and input parameters such as fluid velocity.

Comparing results from the 1-D and 2-D models, it is apparent that the 1-D model is sensitive to permeabilities below 10^{-18} m^2 whereas the 2-D model is not. The causes for this discrepancy are the model geometry and assumptions. In the 2-D model, fluid flowing through the model can avoid the low permeability lens because the hydraulic gradient is never great enough to force fluid through the lens. Instead, the fluid flows around the lens regardless of how low the permeability is set. In contrast, in the 1-D model, the fluid velocity is an input parameter, which strongly affects the helium distribution. As a result, the assumption of a purely vertical hydraulic gradient across the

caprock indicates that the 1-D and 2-D results cannot be compared directly.

Application of quartz-helium method

We assessed the applicability of this method in the context of determining the permeability of shale. The helium concentration in pore water appears to be an effective tool in determining permeability as it allows researchers to find the bulk permeability of a low permeability formation. Helium's diffusive properties will integrate permeabilities over 10's to 100's of meters.

The pore water helium concentration is not one that responds to instantaneous fluctuations in permeability. Consider a caprock that was fractured 1,000 years ago resulting in a significant level of fluid flow containing low amounts of helium: the pore water helium concentration 10 m from the fracture will be virtually unaffected and quartz helium concentrations would show even less of an influence from the fluid flow. Furthermore, the fracturing of the caprock caused by overpressure during carbon sequestration (Streit et al., 2005) would not cause any measureable changes in the spatial distribution of helium for millennia. Therefore it should be stressed that this method is applicable for basins without a recent history of tectonic activity that could have fractured the caprock.

The reliability of pore water helium concentrations using Eqn. 9 is the greatest hindrance to the use of this method. If pore water helium can only be determined within an order of magnitude, spatial variation in concentration may not be resolvable. As a result, permeability may be difficult to assess. Grain coating and low permeability may impede the diffusion of helium between quartz and pore water to the point of equilibrium.

As a result, this method would best be performed on core samples that are sufficiently old and the groundwater flow system has been at steady state for a comparable amount of time. These criteria may considerably decrease the number of basins where this method is appropriate.

Recommendations for future work

Because this study is not fully comprehensive, the following recommendations are suggested for future studies that expand on this idea of quartz grains as *in situ* diffusion samplers:

1) It is recommended that the samples not be heated during any stage aside from helium release and impregnation in sealed vessels. While the diffusivity measurements of Trull et al. (1991) are assumed to be accurate, the potential still exists that a significant amount of helium is being released due to sample heating. Sample desiccation does not require the use of heat and the same results could be obtained using alcohol or acetone.

2) Separating samples into multiple size fractions could be used to assess the degree of degassing during storage and processing as well as assess the degree of equilibrium of helium between quartz and pore water achieved in the subsurface. Ultimately this information could be used as a correction factor. Splitting each sample into a coarse fraction and a fine fraction does double the number of analyses, but because samples can be processed in batch, the analysis time increases only slightly.

3) A sensitivity analysis needs to be performed on site-specific advection-dispersion helium models. Parameters, such as boundary helium concentrations, and measured helium production rates, vary greatly for the Kirtland Formation and greatly affect the

permeability necessary to fit the core sample helium data. This variability, combined with an unknown variability of helium concentrations lateral to the sampling site, opens up the possibility of seal bypass systems that are not being accounted for in 1-D modeling.

4) The modeling of helium migration in real basins suitable for CCS needs to be performed. This is because saline aquifers underlying the caprock may contain high concentrations of helium due to both *in situ* production and a flux from lower sediments or mantle degassing (Ballentine and Burnard, 2002). Helium modeling in this study neglects flux of helium external from the aquifer and instead only accounts for helium originated from *in situ* radiogenic decay; actual case-study application will require consideration of all sources. The $^{3}He/^{4}He$ ratio may prove useful in the determination of permeability. If ^{6}Li, the primary producer of ^{3}He in the crust (Ballentine and Burnard, 2002), concentrations are measured in addition to U and Th concentrations within the caprock, a calculated *in situ* $^{3}He/^{4}He$ ratio could be compared to the quartz or pore water $^{3}He/^{4}He$ ratio. A difference between the two ratios would indicate that helium is being transported into caprock from deeper sources. Knowing the deep source end member $^{3}He/^{4}He$ ratio and flux rate would help provide a permeability estimate. For example, samples from the Kirtland Formation had an average R/R_a value of 0.15 while the average upper crust R/R_a is 0.0078 (Ballentine and Burnard, 2002). This could be an indicator that significant amount of the helium in the Kirtland Formation in fact migrated from sources external to the crust. As a result, the modeling presented above would not be representative of the Kirtland Formation but the expansion of the model would require knowing boundary conditions that cannot be assessed at this time.

5) To assess the effective diffusion time caused by clay and mineral coatings on quartz

grains, bulk core samples could be heated to release all helium before being split into multiple fractions and each fraction impregnated at a different time step before purifying the quartz from the samples and subsequently releasing and analyzing the partitioned helium.

6) If this quartz solubility method is to be compared to the canister method, samples need to be collected in a location where there is no question about the saturation of the pore volume. As demonstrated above, even the slightest degree of unsaturation would cause a substantial increase in apparent dissolved helium using the canister method. As a result it is not possible to definitively compare results from the two methods. As an alternative approach, the quartz solubility method needs to be compared to direct dissolved noble gas measurements collected in a manner that prevents the loss of helium during collection and is not effected by the presence of a gas phase (i.e., Gardner and Solomon, 2009).

CONCLUSIONS

This study has demonstrated the application of quartz-helium solubility with respect to caprock permeability. Caprock bulk permeability is strongly influenced by seal bypass systems such as faults and fractures and this study focuses on constraining that bulk permeability by using helium as a natural tracer. The impregnation experiments performed on Kirtland Formation samples shows that the quartz-air helium isotherm is linear over two orders of magnitude but varies between samples as a result of the fluid inclusion volume. In contrast the high purity quartz from the Spruce Pine Intrusion showed a linear but more variable isotherm. The variability was caused by much lower helium uptake attributed to a lack of fluid inclusions. Pore water helium concentrations that were calculated for the San Juan and Great Artesian Basins using the method of Lehmann et al. (2003) show concentrations greatly exceeding atmospheric solubility but are up to an order of magnitude lower than concentrations measured using the canister method (Gardner et al., submitted; Heath, 2010; Osenbrück et al., 1998). The order of magnitude difference may be caused by helium lost during processing, nonequilibrium between pore water and quartz in the subsurface, or the presence of a gas phase preserved during core collection and subsequently analyzed.

Finite-volume modeling of helium concentrations in a generic sedimentary basin with a low permeability lens indicated that helium is retained due to low fluid velocities while a significant portion of helium is lost through diffusion. Permeability of 10^{-18} and

lower yield nearly identical helium profiles indicating that diffusion is the dominant mechanism of helium transport in very low permeability formations. Due to the low diffusivity of helium in quartz, this method is only applicable to formations that were deposited millions of years ago and the flow system has been quasi-steady state for hundreds of thousands of years. Basin helium modeling could be improved by considering helium sources, external to the basin, that have distinctly different $^{3}He/^{4}He$ ratios. While several other criteria are required for indefinite carbon storage, this study provides a means to constrain the bulk permeability of the caprock while accounting for seal bypass systems that would allow stored fluids to migrate to drinking water supplies and the atmosphere.

APPENDIX

STANDARD OPERATING PROCEDURE

The processing of core samples is relatively straightforward but requires some care in order to preserve quartz grains and trapped helium. This SOP is split into five sections

1) Mineral separation
2) Samplers
3) Evacuation and release
4) Analysis
5) Impregnation

The process from start to finish takes approximately 5 weeks so it is best to process samples in batches. If processing samples in batches, each step will need to be repeated for each sample.

I. Mineral Separation

1. Record the core name and mass.

2. Using a clean mortar and pestle, separate ~50 g of sample and place it in a clean labeled plastic bag. Record the mass.

3. Using a mortar and pestle gently disaggregate the sample into pieces approximately 2 cm across to allow the sample to be placed in the Shatterbox.

4. Place the sample in a clean tungsten carbide Shatterbox sample container. If sample fragments do not fit, return to the previous step.

5. Place the sample container in the Shatterbox, secure it in place and close the lid.

6. Set the Shatterbox for 5 seconds and press Start.

7. Once the Shatterbox has stopped, open the lid and check the sample. If the sample is mostly powder and few pieces larger than 1 cm across, remove the sample from the Shatterbox. If the sample is crushed to a lesser degree, close the Shatterbox and process the sample longer in 5 second intervals.

8. Clean the Shatterbox using warm water and dry thoroughly.

9. Prepare the sieving process by stacking bottom to top, a solid pan, 43 μm, 150 μm, and 850 μm.

10. Add the crushed sample to the 850 μm pan, place the lid on top and shake for 5 seconds. This is enough to separate the larger, uncrushed pieces from the fine fraction.

11. Transfer the >850 μm pieces to the mortar and pestle and crush briefly before repeating the previous step. Continue this cycle until there is not fraction >850 μm.

12. Remove the 850 μm sieve and place the lid on the stack and shake vigorously for 2 minutes. Allow an additional 2 minutes for the dust to settle or work in a fume hood. If the sample will readily disaggregate with the addition of water, wet sieving at this point will remove a lot of clays now and make the process cleaner later. Allow the <44 μm fraction to be washed down the drain. If you choose to wet sieve, dry the sample in the sieves at 50°C for the minimum required time (approximately 30 minutes).

13. Place the 44-150 μm size fraction in a clean plastic bag labeled with the sample name and size fraction. Place the >150 μm size fraction in the original plastic bag and label ">150 μm". If you did not wet sieve, the <44 μm fraction can be retained in a clean plastic bag or discarded.

14. Clean the sieves using hot water and a soft nylon brush.

15. Place the 44-150 μm fraction in a clean 250 mL glass beaker labeled with a permanent marker.

16. In a fume hood, add approximately 25 mL of 10% nitric acid (HNO_3) to the beaker. Be ready for violent effervescence if the sample is high in carbonates.

17. Place the beaker in an ultrasonic bath for 5 minutes. If the beaker is buoyant in the bath, add more HNO_3 or deionized water until the beaker is stable on the bottom of the bath.

18. Remove the beaker and fill with deionized water.

19. The sample will settle out based on grain size and density. In 1 minute is sufficient to settle all grains larger than 44 μm.

20. Decant the beaker retaining all settled sample. At this point it is not necessary to remove all water so it is better to leave some water than to lose the sample.

21. If the water is exceptionally cloudy, repeat the rinse, settle, and decant process

until the water is less turbid.

22. In a fume hood, add approximately 25 mL of 5% hydrofluoric acid (HF) to the beaker.

23. Place the beaker in an ultrasonic bath for 5 minutes. If the beaker is buoyant in the bath, add more HF or deionized water until the beaker is stable on the bottom of the bath.

24. Remove the beaker and fill with deionized water.

25. Allow one minute for the sample to settle.

26. Decant the beaker retaining all settled sample.

27. Repeat the rinse, settle, and decant process until the water runs clear.

28. Fill the beaker with deionized water and place in the ultrasonic bath for 3 minutes.

29. Remove the beaker from the bath and allow 1 minute before decanting. If the water is turbid, clays remain stuck to other mineral grains or clumped together.

30. Continue the use of deionized water and the ultrasonic bath until the water is clear after 1 minute of settling.

31. Decant most water from the beaker and place in an oven at 50°C for approximately 20 minutes to dry the sample completely.

32. Obtain a clean glass slide to which add a small drop of clove oil.

33. Dip a clean needle in the drop of clove oil and then touch the needle to the sample. Transfer this sample to the glass slide and view under a transmitted light microscope with rotating stage. If there are many clear grains, free of opaque coating, the sample is ready for magnetic separation. If the grains all appear clay coated, more HF is required.

34. If the sample is ready for magnetic separation, pour the sample onto a clean sheet of weighing paper to transfer the sample to a clean labeled 10 mL glass vial.

35. Clean the beaker using deionized water and acetone (for the label) and set to dry.

36. Set up the Frantz isodynamic magnetic separator:

    a. Remove the cover and turn on using the switch on the right of the machine near the rear.

    b. Switch the power adjuster to high range using the forward switch on the right of the machine.

c. Set the forward tilt to 20° using the gauge on the back of the machine.

d. Set the side tilt to 10° using the knob on the top right of the machine.

e. Using the knob on the right side (between the two switches you flipped), slowly increase the amperage until the needle gauge reads 1.7.

f. Ensure the cleanliness the track, funnel, and both bins and clean if necessary using a vacuum.

g. Screw the funnel in place until in turns no further.

h. Hang both bins from the two hooks.

i. Ensure the track has the plastic guard in place.

37. Place your sample in the funnel.

38. Turn on the vibrator and set the knob to 8.

39. Slowly unscrew the funnel while watching the outflow onto the track. Unscrew the funnel until the sample is filling the track but you are still able to see the metal of the track (i.e. it should not look like a landslide).

40. Using a piece of tape, secure the funnel in place to prevent it spinning from the vibration, changing the flow rate.

41. When the funnel is empty and no grains are coming down the track, turn the vibrator off and turn the amperage down to zero.

42. Remove the nonmagnetic fraction and place it in a clean 10 mL glass vial labeled: Sample Name non-mag.

43. Replace the nonmagnetic bin on the Frantz and turn the vibrator on to remove magnetite and other strongly magnetic minerals that have remained on the track.

44. View your sample under the microscope using the clove oil technique described above.

45. If the HF clean up was successful, you should have 1-2 grams of clean quartz. If you have a sufficient mass of nonmagnetic sample but other minerals remain such as feldspar, carbon, or pyrite, heavy liquid separation may be your best option.

II. Samplers

1. Mark and cut a piece of straight 1/4” refrigeration grade copper tubing to 16 cm.

2. Clean the piece of tubing using ethyl alcohol and dry thoroughly.

3. With a paintbrush apply a small amount of paste flux to the inside of the tube on one end.

4. Using a bench vice, completely crimp the tube 5 mm from the fluxed end.

5. Apply a small amount of flux to the crimped end.

6. Obtain a beaker filled with cold water, safety glasses, pliers, silver solder, and an oxy-nat gas torch with striker.

7. Lightly clamp the sampler in the bench vice with the crimped end pointing upward.

8. Set the torch so the blue cone is approximately 1 cm long.

9. Solder the crimped end shut.

10. Secure the sampler with the pliers before loosening vice. Quench the sampler in the beaker of cold water.

11. Turn the torch off and proceed to clean the sampler.

12. Fill and rinse the sampler with ethyl alcohol.

13. Refill the beaker with deionized water and set to boil on a hot plate.

14. Place the sampler in the beaker and fill with deionized water.

15. Boil for 10 minutes. During boiling, continue to fill the sampler with deionized water as boiling will push the water out.

16. Remove the sampler from the water and allow to cool.

17. Place a 1/4” 316 Stainless Steel 37° AN fitting on the tubing and flare the un-crimped end using a 37° flaring tool.

18. Flaring the tubing will leave a small burr on the inside of the tubing. Place a #12 drill bit in the drill press to which add a drop of cutting oil. Hold the sampler aligned with the drill bit and drill down 5 mm to remove the burr.

19. Clean the cutting oil from the sampler using ethyl alcohol. Roll a lint-free wipe and insert completely into the sampler using a twisting motion.

20. When the interior of the sampler is as clean as possible, rinse once more in ethyl alcohol and dry completely using compressed air with a needle output.

21. Measure 6 cm from the base of the end crimp and mark.

22. Using a pipe-cutting tool fitted with a crimping wheel, lightly crimp at the 6 cm

mark. This crimp will act as a stop for the frit you will insert later.

23. Scribe the sample name into the sampler using an engraver. Place the name between the crimp and the soldered end to avoid affecting the clamping zone.

24. Obtain a 0.187" diameter stainless steel 10 micron grade frit and weight it along with the sampler. Record "mass sampler:" followed by the mass from the analytical balance.

25. Insert sample into the sampler.

    a. Hold the sampler vertically with the open end facing upward. Use a tubing rounder and a lab jack to help position the sampler.

    b. Insert a piece of 1/8" plastic tubing fitted with a small funnel drilled out with a #31 drill bit allowing the funnel to fit over the tubing.

    c. Measure out approximately 1 gram of quartz on a piece of weighing paper.

    d. Pour the sample into the funnel.

    e. Tap the side of the funnel and sampler to coax the quartz into the sampler as the static charge will cause the sampler to stick to the plastic.

    f. Remove the funnel and check for quartz grains stuck inside the sampler near the opening. Gently remove them using a lint-free wipe.

    g. Carefully insert the frit squarely into the sampler. Use a long stainless steel rod to help coax the frit into the sampler until it stops at the crimp. Using the rod as a depth gauge, check that the frit is in place.

    h. Using the pipe-crimper secure the frit in place approximately 2 mm from the previous crimp.

    i. Using compressed air blow out the sampler to remove any quartz that remains above the frit.

    j. Gently wipe the inside of the sampler using a clean lint-free wipe.

26. Reweigh the sampler on the analytical balance and record: "mass full:" and the measurement. Take the difference between mass full and mass sampler and record: "mass quartz:" and that value.

III. Evacuation and release

This section of the SOP is designed for use at the Dissolved and Noble Gas Laboratory at the University of Utah, but could be adapted to any laboratory with a similar vacuum

line. Two samples can be evacuated at the same time utilizing both Nupro valves (see diagram below). This tutorial assumes you are only preparing one sample.

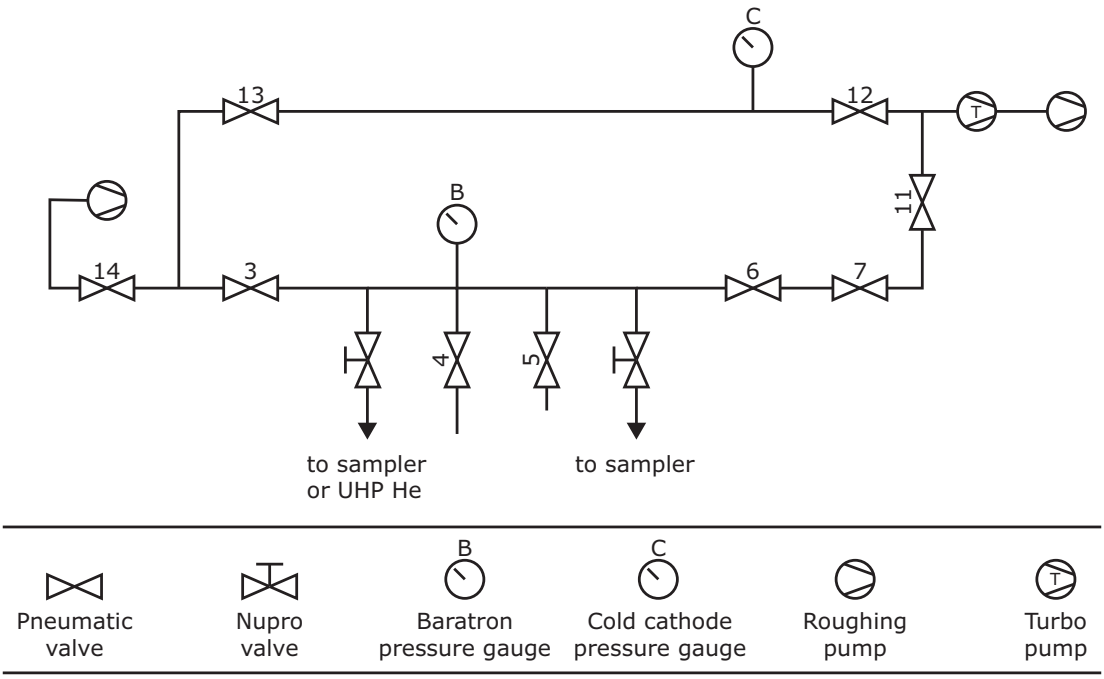

Extraction Line Schematic

1. Go to the extraction line.
2. Close the Nupro valve on the right and unscrew the cap on the AN fitting.
3. Install the sample to the proper tightness.
4. Make sure that valves 13, 6, and 7 are closed.
5. Open valve 14 if it is not open already.
6. Ensure that all ports are plugged and open valve 3 followed by the Nupro valve your sample is installed on.
7. Assuming that the turbo pump is not turned on, turn it on. Wait 2 seconds after you hear the pump start up and open valves 11 and 12.
8. Wait until the cold cathode pressure reads in the 10^{-6} Torr range.
9. If the Baratron pressure is below 0.5 Torr, close valve 3.
10. If the Baratron pressure does not rise quickly, open valves 6 and 7.

11. Record the date and time preceded by “Turbo’ed:”.

12. The sample needs to be pumped down for 24 hours. In the meantime occasionally check on both the Baratron pressure and the cold cathode pressure. The Baratron should steadily decrease to 0.000 within a few hours. The cold cathode should steadily decrease into the low 10^{-7} range or the high 10^{-8}. If the sample is not pumping down, there may be a small leak in the solder or a leak at the flare. Close the Nupro valve and valves 6 and 7. Remove the sampler to inspect for leak sources. When you are done, replace the sampler and open valve 3 followed by the Nupro valve. When the Baratron pressure reaches below 0.5 Torr, close valve 3 followed by opening valves 6 and 7. Remember that if you remove the sampler you will need to rerecord the turbo start time.

13. After 24 hours check the cold cathode pressure which should be below 5.0×10^{-8} Torr. If the pressure is not this low, a leak may exist or the sample just needs more time to degas. You will have to use your own reasoning to assess the problem.

14. Using a stainless steel pinch clamp designed for copper tubing, seal the sampler 2 cm from the crimp. Make sure that the tubing is centered in the clamp and is installed straight. Use 5/8” and 9/16” wrenches to complete this task.

15. Record the seal date and time after the start time. Follow this record with the final cold cathode pressure.

16. Close the Nupro valve and unscrew the sample.

17. Purge the open end of the sampler with dry nitrogen and immediately insert a stainless steel AN plug into the fitting and tighten properly. These two measures will prevent oxidation inside of the tubing while it sits in the oven.

18. If you are continuing to evacuate additional samplers, repeat the steps above. If you are done, close valves 6 and 7 followed by valves 11 and 12. Turn the turbo off.

19. If necessary create an oven sample sheet with the column headers:
    Sample Date In Date Out Impreg? Location

20. Ensure that the oven temperature is stable at 290°C.

21. Record the sample name and the date and time. Under Impreg? Put a dash indicating that the sample is not being impregnated.

22. Quickly open the oven and place the sampler in an available spot. Avoid creating multiple rows back into the oven as these samplers will be difficult to remove when the samplers are 290°C and 290°C samplers are blocking your approach.

23. Close the oven and record where in the oven the sampler was placed using a

simple convention.

24. After 10 days, record the date and time. Remove the sampler using a heatproof glove and place the sampler on the counter away from all objects and other laboratory activity.

IV. Analysis

The samples will be analyzed using a Tank 2 Standard (Diffusion Samplers). Below are the steps that are different from running Advanced Samplers.

1. Cap the A and B ports with standard caps.

2. Pump the ports down and run two Tank 2 Standards.

3. Record the mass of quartz in Batchwater.

4. Install samples on ports A and B and pump down.

5. When it is time, carefully break the bolts. Significant force may be necessary as the heat of the oven has dried the antiseize compound.

6. Completely reround the tubing at the site of clamping. The tubing will be considerably brittle from the heat treatment. You will hear and feel a *crack* when the sampler walls finally separate. If you do not hear a crack or the pressure does not rise, vice grips will readily separate the walls. The water inlet pressure will range between 0.1 and 4 Torr for an initial release. For a post impregnation release the pressure should be below 0.05 Torr unless a leak occurred during the release stage.

7. Allow the pressure to stabilize before proceeding.

8. Add fresh antiseize compound to the bolt threads and after the process allows you to install a new set of samples, clamp the sampler off 3 cm from the base of the AN fitting.

Note that it may be necessary to run a blank run if helium release is low.

V. Impregnation

You will be using the extraction line used for evacuations (see diagram above).

1. Close both Nupro valves and open valves 3, 4, and 5.

2. Attach an analyzed sample to the right Nupro valve and open that valve.

3. Remove the clamp and fully reround the tubing. Allow the sample to pump down to base level.

4. Attach a length of 1/4” tubing fitted with an AN fitting and a 1/4 turn valve to a Ultra High Purity Helium tank complete with regulator.

5. Attach the free AN fitting to the left Nupro valve port but do not open the valve.

6. When the sampler has pumped down to base level (0.000 Torr on the Baratron), close the right Nupro valve and valves 4 and 5.

7. Open the left Nupro valve to pump down the regulator and extension tubing. Open the 1/4 turn valve as well. The regulator will not hold vacuum so the Baratron will not go to base at this point.

8. Unscrew the pressure regulator all the way but before the handle unscrews from the body.

9. In quick succession, close the 1/4 turn valve, close the Nupro valve and open the valve on the helium tank. Slowly turn the pressure regulator handle until the needle reads 20 psi.

10. When the Baratron is back to base level, open valves 4 and 5 and the right Nupro valve.

11. Close valve 3.

12. Open the 1/4 turn valve and wait 5 seconds. Close the 1/4 turn valve and open the left Nupro valve. Wait 5 seconds before closing the valve. The high range Baratron should read HI $x10^2$ meaning that the line pressure is above 100 Torr.

13. Open valve 3 and pump away all helium until the Baratron reaches base again.

14. As above, close valve 3. Open the 1/4 turn valve for 5 seconds and then close it. Open the left Nupro valve, wait 5 seconds and then close it.

15. Close the right Nupro valve and valves 4 and 5.

16. Open valve 3 and pump the line to base pressure.

17. Close valve 3 and open the right Nupro valve. The pressure will be above the low range Baratron but should read on the high range Baratron. The goal at this point is to get the line pressure (and the sampler pressure) to 10 Torr.

18. Open valves 4 and 5 and allow the pressure to stabilize. This pressure is above 10 Torr and you will need to experiment with pumping away fractions of gas while keeping gas in the sampler and behind valves 4 and 5. With some practice it is simple to get the pressure you desire ± 10%. Note that you should not dynamically pump on gas that you are keeping, as fractionation will occur. You may have to return to step 13 if you have pumped away too much gas.

19. When you are satisfied with the Baratron pressure, clamp the sampler shut centered between the two previous clamp locations.

20. Record the final Baratron pressure as the pressure has risen through clamping and compressing the gas.

21. Close the right Nupro valve and remove the sampler.

22. If necessary create an oven sample sheet with the column headers:
    Sample Date In Date Out Impreg? Location

23. Ensure that the oven is set and is stable at 290°C.

24. Record the sample name and the date and time. Under Impreg? Put a check indicating that the sample is being impregnated.

25. Quickly open the oven and place the sampler in an available spot. Avoid creating multiple rows back into the oven as these samplers will be difficult to remove when the samplers are 290°C and are blocking your approach.

26. Close the oven and record where in the oven the sampler was placed using a simple convention.

27. After 10 days, record the date and time. Remove the sampler using a heatproof glove and place the sampler on the counter away from all objects and other laboratory activity.

28. Once the sampler has cooled, the contents will need to be transferred to a new weighed and labeled sampler. Refer to steps 1-24 in Section 2 if samplers need to be made.

29. Set up to fill the sampler as described in step 25a-b of Section 2.

30. Clean the loose oxidation from the surface of the sampler using a lint-free wipe and steel wool.

31. Using wire cutters remove the end of the sampler just below the soldered crimp.

32. Using a bench vice, reround the sampler. If the sampler does not readily reround, it is still soldered shut. Cut the sampler 1-2 mm lower using the wire cutters and repeat with the bench vice.

33. While holding the sampler vertically, remove any oxidation that loosened through rerounding.

34. Pour the contents of the sampler into the funnel. Tap the side of the sampler to ensure that all quartz has come out of the sampler.

35. Complete the process by following Steps 25e-26 of Section 2 and continuing to

Section 3 to pump the sample down.

REFERENCES

Ballentine, C. J., and Burnard, P. G., 2002, Production, release and transport of noble gases in the continental crust, *in* Porcelli, D., Ballentine, C. J., and Wieler, R., eds., Reviews in Mineralogy and Geochemistry, Volume 47: Washington, DC, Mineralogical Society of America, Geochemical Society, p. 481-538.

Baxter, E. F., 2010, Diffusion of noble gases in minerals, *in* Zhang, Y., and Cherniak, D. J., eds., Reviews in Mineralogy and Geochemistry, Volume 72: Washington, DC, Mineralogical Society of America, Geochemical Society, p. 509-557.

Bethke, C. M., Zhao, X., and Torgersen, T., 1999, Groundwater flow and the 4He distribution in the Great Artesian Basin of Australia: Journal of Geophysical Research, v. 104, no. B6, p. 12999-13011.

Bodnar, R. J., 2003, Introduction to fluid inclusions, *in* Samson, I., Anderson, A., and Marshall, D., eds., Fluid inclusions analysis and interpretation, Volume 32: Vancouver, Mineralogical Association of Canada, p. 1-8.

Brooker, R. A., Wartho, J. A., Carrol, M. R., Kelley, S. P., and Draper, D. S., 1998, Preliminary UVLAMP determinations of argon partition coefficients for olivine and clinopyroxene grown from silicate melts, *in* Carrol, M. R., Kohn, S. C., and Wood, B. J., eds., The Degassing of the Earth: Amsterdam, Elsevier, p. 185-200.

Cerling, T. E., 1990, Dating geomorphologic surfaces using cosmogenic ^{3}He: Quaternary Research, v. 33, p. 148-156.

Crank, J., 1975, The Mathematics of Diffusion, Oxford, Clarendon.

Farley, K. A., 2000, Helium diffusion from apatite: general behavior as illustrated by Durango fluorapatite: Journal of Geophysical Research, v. 105, p. 2903-2914.

Fassett, J. E., and Hinds, J. S., 1971, Geology and fuel resources of the Fruitland Formation and Kirtland Shale of the San Juan Basin, New Mexico and Colorado: U.S. Geological Survey Professional Paper 676, p. 76.

Gardner, W. P., Harrington, G. A., and Smerdon, B. D., 2012, Using terrigenic ^{4}He to quantify variability in aquitard leakage: Submitted to Journal of Hydrology.

Gardner, W. P., and Solomon, D. K., 2009, An advanced passive diffusion sampler for the determination of dissolved gas concentrations: Water Resources Research, v.

45, p. W06423.

Graham, T., 1864, On the molecular mobility of gases: Journal of the Chemical Society of London, v. 17, p. 334-339.

Heath, J. E., 2010, Multi-scale petrography and fluid dynamics of caprocks associated with geologic CO_2 storage [Ph.D. Dissertation]: New Mexico Institute of Mining and Technology.

Hendry, M. J., Kotzer, T. G., and Solomon, D. K., 2005, Sources of radiogenic helium in a clay till aquitard and its use to evaluate the timing of geologic events: Geochimica et Cosmochimica Acta, v. 69, no. 2, p. 475-483.

IPCC, 2005, IPCC special report on cardon dioxide capture and storage, Cambridge, United Kingdom and New York, NY, USA, Cambridge University Press, 442 p.:

Jahne, B., Heinz, G., and Dietrch, W., 1987, Measurement of the diffision co-efficients of sparingly soluble gases in water: Journal of Geophysical Research, v. 92, p. 10767-10776.

Kaiser, W. R., Swartz, T. E., and Hawkings, G. J., 1994, Hydrologic framework of the Fruitland Foramtion, San Juan Basin, *in* Ayers, W. B., and Kaiser, W. R., eds., Coalbed Methane in the Upper Cretaceous Fruitland Formation, San Juan Basin, New Mexico and Colorado, New Mexico Bureau of Mines and Mineral Resouces Bulletin, Volume 146, p. 187-207.

Kernodle, J. M., 1996, Hydrogeology and steady-state simulation of ground-water flow in the San Juan Basin, New Mexico, Colorado, Arizona, and Utah: U.S. Geological Survey Water-Resources Investigations Report 95-4187.

Kipfer, R., Aeschbach-Hertig, W., Peeters, F., and Stute, M., 2002, Noble gases in lakes and ground waters *in* Porcelli, D., Ballentine, C. J., and Wieler, R., eds., Noble Gases in Geochemistry and Cosmochemistry, Volume 47: Washington, D.C., Mineralogical Society of America, Geochemical Society, p. 615-700.

Lehmann, B. E., Waber, H. N., Tolstikhin, I., Kamensky, I., Gannibal, M., and Kalashnikov, E., 2003, Helium in solubility equilibrium with quartz and porefluids in rocks; a new approach in hydrology: Geophysical Research Letters, v. 30, no. 3, p. 4.

Mamyrin, B. A., and Tolstikhin, I., 1984, Helium isotopes in nature, Developments in Geochemistry, Volume 3: New York, Elsevier Science, p. 273.

Mazor, E., 1995, Stagnant aquifer concept; Part 1, Large-scale artesian systems; Great Artesian Basin, Australia: Journal of Hydrology, v. 173, no. 1-4, p. 219-240.

Mazor, E., and Nativ, R., 1994, Stagnant groundwater stored in isolated aquifers: implications related to hydraulic calculations and isotope dating; reply: Journal of

Hydrology, v. 154, no. 1-4, p. 409-418.

Niedermann, S., 2002, Cosmic-ray-produced noble gases in terrestrial rocks: dating tools for surface processes, *in* Porcelli, D., Ballentine, C. J., and Wieler, R., eds., Reviews in Mineralogy and Geochemistry, Volume 47: Washington, DC, Mineralogical Society of America, Geochemical Society, p. 731-784.

Oldenburg, C., and Pruess, K., 1995, EOS7R: Radionuclide Transport for TOUGH2.

Osenbrück, K., Lippman, J., and Sonntag, C., 1998, Dating very old pore waters in impermeable rocks by noble gas isotopes: Geochimica et Cosmochimica Acta, v. 62, no. 18, p. 3041-3045.

Pruess, K., Oldenburg, C., and Moridis, G., 1999, TOUGH2 User's Guide, Version 2.0.

Roedder, E., 1984, Fluid Inclusions, Mineralogical Society of America Reviews in Mineraology, 644 p.:

Romm, E. S., 1966, Flow characteristics in fractured rocks (in Russian), Moscow, Nedra.

Rosenblum, S., 1958, Magnetic susceptibilities of minerals in the Frantz isodynamic magnetic separator: The American Mineralogist, v. 43, p. 170-173.

Rübel, A. P., Sonntag, C., Lippman, J., Pearson, F. J., and Gautschi, A., 2002, Solute transport in formations of very low permeability: Profiles of stable isotopes and dissolved noble gas contents of pore water in the Opalinus Clay, Mont Terri, Switzerland: Geochimica et Cosmochimica Acta, v. 66, no. 8, p. 1311-1321.

Schlosser, P., 1992, Tritium/^{3}He dating of waters in natural systems, Isotopes of Noble Gases as Tracers in Environmental Studies, Proceedings of a Consultants Meeting on Isotopes of Noble Gases as Tracers in Environmental Studies, May 29–June 2, 1989: Vienna, IAEA, p. 123-147.

Schlosser, P., Stute, M., Dorr, H., Sonntag, C., and Munnich, K. O., 1988, Tritium/^{3}He dating of shallow groundwater: Earth and Planetary Science Letters, v. 89, no. 3-4, p. 353-362.

Schwartz, F. W., and Zhang, H., 2003, Fundamentals of Ground Water, New York, NY, John Wiley & Sons, Inc.

Shepard, R. G., 1978, Underground water resources of South Australia, Volume 48: Adelaide, Geological Survey of South Australia, p. 66.

Shuster, D. L., and Farley, K. A., 2005, Diffusion kinetics of proton-induced 21Ne, 3He, 4He in quartz: Geochimica et Cosmochimica Acta, v. 69, p. 2349-2359.

Solomon, D. K., 2000, ^{4}He in groundwater, *in* Cook, P. G., and Herczeg, A. L., eds., Environmental Tracers in Subsurface Hydrology, Kluwer Academic Publishers, p.

425-439.

Solomon, D. K., and Cook, P. G., 2000, ^{3}H and ^{3}He, *in* Cook, P. G., and Herczeg, A. L., eds., Environmental Tracers in Subsurface Hydrology: Boston, Kluwer Academic Press, p. 397-424.

Streit, K., Siggins, A., and Evans, B., 2005, Predicting and monitoring geomechanical effects of CO_2 injection, Carbon Dioxide Capture for Storage in Deep Geologic Formations—Results from the CO_2 Capture Project,, *in* Benson, S., ed., Geologic Sotrage of Carbon Dioxide with Monitoring and Verification, Volume 2: London, Elsevier Science, p. 751-766.

Stute, M., Sonntag, C., Deák, J., and Schlosser, P., 1992, Helium in deep circulating groundwater in the Great Hungarian Plain; flow dynamics and crustal and mantle helium fluxes: Geochimica et cosmochimica acta, v. 56, no. 5, p. 2051-2067.

Swanson, S. E., and Veal, W. B., 2010, Mineralogy and petrogenesis of pegmatites in the Spruce Pine District, North Carolina, USA: Journal of Geosciences, v. 55, p. 27-42.

Tolstikhin, I., Gannibal, M., Tarakanov, S., Pevzner, B., Lehmann, B., Ihly, B., and Waber, H. N., 2005, Helium transfer from water into quartz crystals: A new approach for porewater dating: Earth and Planetary Science Letters, v. 238, p. 31-41.

Torgersen, T., and Clarke, W. B., 1985, Helium accumulation in groundwater, I: An evaluation of sources and the continental flux of crustal ^{4}He in the Great Artesian Basin, Australia: Geochimica et Cosmochimica Acta, v. 49, p. 2445-2452.

Tóth, J., 1963, A theoretical analysis of groundwater flow in small drainage basins: Journal of Geophysical Research, v. 68, p. 4795-4812.

Trull, T. W., Kurz, M. D., and Jenkins, W. J., 1991, Diffusion of cosmogenic ^{3}He in olivine and quartz; implications for surface exposure dating: Earth and Planetary Science Letters, v. 103, no. 1-4, p. 241-256.

Zheng, L., Apps, J. A., Zhang, Y., Xu, T., and Birkholzer, J. T., 2009, On mobilization of lead and arsenic in groundwater in response to CO_2 leakage from deep geological stoarge: Chemical Geology, v. 268, no. 3-4, p. 281-297.

Zhou, Z., and Ballentine, C. J., 2006, He-4 dating of groundwater associated with hydrocarbon reservoirs: Chemical Geology, v. 226, p. 309-327.